https://doi.org/10.1016/j.jweia.2023.105537

Evolution of flow field around high-speed trains meeting at the tunnel entrance under strong wind-rain environments

De-Hui Ouyang[a], E Deng[b,c,*], Yi-Qing Ni[b,c], Wei-Chao Yang[a,d], Zheng-Wei Chen[b,c]

a School of Civil Engineering, Central South University, Changsha, People's Republic of China;

b National Rail Transit Electrification and Automation Engineering Technology Research Center (Hong Kong Branch), Hong Kong, People's Republic of China;

c Department of Civil and Environmental Engineering, The Hong Kong Polytechnic University, Hong Kong, People's Republic of China.

d National Engineering Research Center of High-speed Railway Construction Technology, Changsha, People's Republic of China;

* Corresponding author. E-mail address: early.deng@polyu.edu.hk

Abstract: Tropical storms pose a great threat to the traffic safety of tunnel-embankment transition sections in coastal areas, especially when two trains are meeting. A series of 3D computational fluid dynamics numerical simulations of wind-rain-tunnel-embankment-train are established using the Eulerian multiphase and the Shear-Stress Transport k-ω models. The numerical model's reliability is verified by wind tunnel tests using rainfall simulation technology. The differences in the train's aerodynamic performance before and during the meeting under different wind-rain conditions are analyzed. The rain phase's impact mechanism on the flow field is revealed. Results show that: Before the meeting, the rain phase will worsen the train's aerodynamic performance. When the wind speed and rainfall intensity is 20 m/s and 400 mm/h, the head train's average lift force ($\overline{C}_y$), yawing and pitching moments ($\overline{C}_{mz}$) increase by 6.25%, 9.68% and 10.31%, respectively. The rain phase increases the wind-rain load amplitude during the meeting, and the head train's pitching moment increases by 10.7%. The moment is more worthy of attention than that of force under

a rainy day, and the change rate of $\overline{C}_{mz}$ is 4.9 times of that of $\overline{C}_{y}$. The amplification effect of rain on wind-rain loads may endanger the driving safety of trains at the tunnel entrance.

Key words: strong wind-rain environment; tunnel-embankment section; two high-speed trains meeting; Eulerian multiphase model; transient aerodynamic performance

1. Introduction

There have been a number of train accidents in strong winds around the world (Andersson et al., 2004). Now, global warming has led to increased damage to infrastructure by tropical storms along the coasts of eastern Asia and western Europe (Jian et al., 2022). According to the statistical study conducted by Liu et al. (2021), there were about 975 railway disasters caused by heavy rainfall in China during 1981-2016. Therefore, extreme natural weather, such as strong winds and heavy rain caused by tropical storms, has become a major source of risk affecting the safe operation of high-speed trains (HST) (Montenegro et al., 2020(a); Mohebbi et al., 2013, 2018a; Ottar et al., 2023). The tunnel-embankment transition section is in the weak zone of the operation environment due to the rapid change in the infrastructure structure. This leads to dramatic changes in the train's wind-rain loads in a very short period of time. Therefore, it is of great significance to grasp the change law of the wind-rain loads of the carriage under the coupling of wind-rain phases and the spatial distribution law of wind-rain phases around the train to ensure the safe operation of high-speed trains.

At present, in the study of aerodynamic performance of HST under crosswind environments (Mohebbi et al., 2021, 2022), some researchers pay attention to the energy dissipation shielding effect of anti-wind structure on incoming flow on the windward side of trains (Mohebbi et al., 2017, 2018b). Many scholars are currently studying the aerodynamic characteristics of trains under pure crosswinds (Li et al.,

2023; Liang et al., 2023), which are reflected in wind tunnel tests or numerical simulations of flat ground, embankments and bridges (Chen et al., 2018; Noguchi et al., 2019; Montenegro et al., 2020(b)). Some researchers have also found that differences in wind models can also significantly affect the aerodynamic characteristics of trains. Neto et al. (2021) systematically studied the regularity of different wind directions on the safety of trains, and the wind contour line was generated based on the Chinese cap model. The results showed that vertical wind direction is the greatest threat to the safe operation of trains. Han et al. (2020) compared the effects of steady and unsteady aerodynamic loads on the dynamic response index of trains running on bridges and found that considering the pulsating components in the crosswind flow is more conducive to evaluating the operational safety of trains. Yang et al. (2022a) also compared the difference in flow fields around trains under reconstructed natural wind and steady wind conditions in the tunnel-bridge section. It can be seen that great progress has been made in the relevant research, considering pure crosswind simulation methods and different infrastructure factors.

Wind-driven rain (WDR) are raindrops that obtain horizontal speed when driven by wind power. For wind-rain two-phase flow, researchers mainly use the computational fluid dynamics (CFD) technique using the Eulerian multiphase (EM) model and the wind tunnel test method using the spray device (Zeng et al., 2023). In the current wind-rain numerical simulation techniques, due to the randomness of the initial conditions of raindrops, a large number of calculations are required on the raindrop trajectories to obtain the distribution of capture rates. Jiang et al. (2016) proposed a new method to obtain the capture rate distribution by the finite surface element method, which reduced the computational amount of raindrop trajectories and

the randomness of the capture rate distribution. In order to more accurately predict the influence of wind-rain on the wetness distribution of the façade of buildings, Kubilay et al. (2015) proposed a method to achieve turbulent diffusion in the EM model. Wind-rain simulation is mainly used in the study of rainwater intrusion into the external walls of buildings and the dynamic response of raindrops impacting structures in a typhoon environment (Huang et al., 2012; 2019). However, some researchers have carried out related studies on the train's aerodynamic characteristics in heavy wind-rain cases. Shao et al. (2011) studied the wind-rain loads under wind-rain environments based on the EM model and concluded that the train's resistance, lateral and lift forces are greater under rainy conditions than under rainless conditions, and the difference increases with the incoming flow speed. Li et al. (2019) investigated the train's aerodynamic performance under the wind-rain coupling based on the Euler-Lagrangian method, and the findings revealed that the raindrops accelerate the airflow around the train while inhibiting the vortex degeneration, which will lead to an increase in fluid flow velocity around the train with the increase in rainfall. Some researchers have begun to pay attention to the influence of raindrop simulation methods on the aerodynamic coefficients of trains. For example, Yu et al. (2021) discussed the usefulness of the raindrop shape hypothesis. The team also studied the train's aerodynamic coefficients using the non-spherical raindrop model, and the results indicated that the density of raindrops around the train is positively correlated with the rainfall intensity (Yu et al., 2022). On the basis of researching the aerodynamic load of trains, Gou et al. (2021) further addressed the impact of wind-rain on the train-track-bridge dynamic response system. The findings indicate that the rainfall intensity has significant effect on the dynamic response of the train.

Although the above researchers have carried out different degrees of research on

the train's aerodynamic characteristics under the coupling of wind-rain and achieved certain results, there are still some problems that need to be solved. First of all, their research subject is mainly a train, and the complex aerodynamic characteristics of trains meeting are overlooked (Wang et al., 2019; Yang et al., 2022b). Secondly, under the coupling of wind-rain, the rain phase will affect the incoming flow's velocity and turbulence intensity (Zeng et al., 2023), but the above studies are based on the steady-state or quasi-steady-state assumption, that is, the train is stationary or only uses the simulation method of ground or bridge deck movement, and the results are relatively conservative (Krajnovic´ et al., 2012; Dorigatti et al., 2015). In fact, in the study of the transient aerodynamic effect of HSTs under a pure crosswind environment, some researchers based on wind tunnel tests and CFD simulations revealed that there is an acceleration effect on crosswinds at the tunnel entrance and high-speed trains traveling through tunnel openings produce complex aerodynamic abrupt behavior (Wang, et al., 2021; Zhou, et al., 2021; Yang et al., 2022c). In addition, the train's aerodynamic change behavior is aggravated by the pulsating impact of two trains traveling in opposite directions. As a result, it is especially important to investigate the aerodynamic characteristics of trains passing each other and the spatial evolution rule of two-phase around the train in a wind-rain environment at the tunnel entrance, which is also one of the purposes of this study.

In this study, a series of 3D wind-rain-tunnel-embankment-train CFD numerical dynamic models are established based on the EM and Shear-Stress Transport (SST) *k*-ω turbulence models. Firstly, the turbulence model's accuracy and the multiphase flow model using raindrop grouping are verified by wind tunnel tests. Secondly, the transient aerodynamic differences in the meeting process under different wind speed and rainfall intensity conditions are analyzed, including the average wind-rain loads

and its amplitude. The temporal and spatial distribution laws of the two phases around the train body with the change of rainfall intensity and wind speed are studied, and the rain phase's impact mechanism on the wind-rain loads and separation vortex is revealed by the flow field. The structure of the article is arranged as follows: The second section introduces the geometric model, boundary conditions, mesh method, rain phase model and working condition arrangement. The third section mainly analyzes the differences in aerodynamic characteristics under different rainfall intensity and wind speed conditions, displays the spatial distribution law of the two phases by the flow field, and reveals the mechanism of aerodynamic load differences. This paper's primary contribution is to reveal the aerodynamic characteristics and time-varying characteristics of the rain phase when two trains meet under strong wind-rain environments.

2. Numerical model methods

2.1. Wind-rain phase model

At present, there are two main numerical methods for simulating wind-rain environment: the discrete particle model (DPM) and the EM model. Due to the huge CPU resource consumption and computing memory space, DPM is difficult to use in large engineering numerical models. Therefore, the EM model is used in the paper, which has been used by some researchers to research the train's aerodynamic performance under wind-rain conditions (Shao et al., 2011). Under the action of crosswind, the tracks of raindrops with different particle sizes are different (Zeng et al., 2023), so their effects on the aerodynamic performance of the carriage are also different. Therefore, rain phases with different particle sizes should be considered in the model. In the EM model, both the air and rain phases are treated as independent parts of the continuum. Considering that raindrops tend to break into small raindrops

in the air after reaching 6 mm in diameter, the particle size of the rain phase is divided into 6 groups, and the intermediate particle size of each group is used as a representative value. For example, the particle size in the first group is $D_1 = 0.5$ mm, and the particle size range is 0~1 mm. The mass and momentum equations for the rain phase are shown in Eqs. 1 and 2 (Kubilay et al., 2013). The relation between the volume fraction of wind phase and rain phase is shown in Eq. 3. Based on the Navier-Stokes equations, the governing equation of wind phase is shown in Eqs. 4-7.

$$\frac{\partial \rho_w \alpha_k}{\partial t} + \frac{\partial (\rho_w \alpha_k u_{k,j})}{\partial x_j} = 0, \tag{1}$$

$$\frac{\partial \rho_w \alpha_k u_{k,i}}{\partial t} + \frac{\partial (\rho_w \alpha_k u_{k,i} u_{k,j})}{\partial x_j} = \rho_w \alpha_k g + \rho_w \alpha_k \frac{3\mu}{\rho_w D_k^{\,2}} \frac{C_D Re_p}{4} (u_i - u_{k,i}), \tag{2}$$

$$\sum_{k=1}^{n} \alpha_k + \alpha_a = 1, \tag{3}$$

$$\frac{\partial u_j}{\partial x_j} = 0, \tag{4}$$

$$\frac{\partial \rho u_i}{\partial t} + \frac{\partial \rho u_i u_j}{\partial x_j} = -\frac{\partial p}{\partial x_i} + \frac{\partial \tau_{ji}}{\partial x_j} + S_{li}, \tag{5}$$

$$\frac{\partial \rho k}{\partial t} + \frac{\partial \rho k u_j}{\partial x_j} = \frac{\partial}{\partial x_j}\left[\left(\mu + \frac{\mu_t}{\sigma_k}\right)\frac{\partial k}{\partial x_j}\right] + G_k - \rho\varepsilon, \tag{6}$$

$$\frac{\partial \rho \varepsilon}{\partial t} + \frac{\partial \rho \varepsilon u_j}{\partial x_j} = \frac{\partial}{\partial x_j}\left[\left(\mu + \frac{\mu_t}{\sigma_\varepsilon}\right)\frac{\partial \varepsilon}{\partial x_j}\right] + \rho C_1 S\varepsilon - \rho C_2 \frac{\varepsilon^2}{k + \nu\varepsilon}, \tag{7}$$

where α_k represents the volume fraction of *k*th rain phase; α_a represents the volume fraction of air; μ represent the dynamic viscosity; $u_{k,i}$, $u_{k,j}$ represent the velocity of the *i* and *j* directions in the *k*th phase, respectively; ρ_w represents the raindrop's density; g represents the gravitational acceleration; C_D and Re_p represent the drag coefficient and the relative Reynolds number, respectively. S_{li} represent the momentum contribution of rain to air.

The volume fraction of raindrops with different diameters is different under different rainfall intensity. The distribution function of Marshall-Palme (M-P) is an earlier proposed raindrop spectrum, but it has some problems that lead to its limited range of use. Another widely used raindrop spectrum is the Gamma distribution, which is essentially a correction of the M-P distribution. In order to simulate the rain phase more accurately, the modified Gamma distribution form is used, and its functions are shown in Eqs. 8 and 9 (Wolf D., 2001; Huang et al., 2012).

$$N(D)=N_0 D^{2.93}\exp(-5.38I^{-0.186}D)\,, \tag{8}$$

$$N_0=1.98\times10^{-5}I^{-0.384}\,, \tag{9}$$

where, I denotes the rain intensity.

Rainfall intensity (I), volume fraction (α_k), and rain phase fall speed $V_t(D)$ are the key parameters of wind and rain simulation. Considering the coastal typhoon-prone areas, heavy rainfall can even reach 400 mm/h in a short period of time (Yang et al., 2021). Therefore, the rainfall intensity in this paper is 100 mm/h, 200 mm/h, 300 mm/h and 400 mm/h. After determining the rainfall intensity, the volume fraction of raindrops with different diameters can be obtained by Eqs. 10 and 11, and the final falling speed of raindrops can be determined by Eq. 12 (Gunn and Kinzer, 1949).

$$\alpha_k=\frac{If(I,D)\times10^{-3}}{V_t(D)\times3600}\,, \tag{10}$$

$$f(I,D)=\frac{D^3N(I,D)V_t(D)}{\int_0^\infty D^3N(I,D)V_t(D)\mathrm{d}D}\,, \tag{11}$$

$$V_t(D)=\begin{cases}0;\ \ D\le0.03\ \text{mm}\\ 4.323(D-0.03);0.03\ \text{mm}<D\le0.6\ \text{mm}\\ 9.65-10.3e^{-0.6D};D>0.6\ \text{mm}\end{cases}\,, \tag{12}$$

2.2. Turbulence model

Researchers often use four turbulence models, such as the Renormalization

Group (RNG k-ε), SST k-ω, improved delayed detached eddy simulation (IDDES) and large eddy simulation (LES), to study the train's aerodynamic performance. Among them, the IDDES and LES models are often used for scaled models because of their extremely high requirements for the grid size of train walls and large computing resources. Although the computational accuracy of the RNG k-ε turbulence (Rezvani et al., 2014) model can meet the needs of engineers, its ability to simulate separated flows is weak, and it is not suitable for observing the development and change of separation vortices around the train. The SST k-ω turbulence model can meet this point well, and the computing resource consumption is within an acceptable range. This turbulence model is also used by researchers to study the development of flow around the train (Li et al., 2019) and wind and rain simulation (Yu et al., 2021). Therefore, the separation and distribution of wind and rain phases around the train are researched using the SST k-ω model. It is expressed in the following form (Menter, 1994).

$$\rho\frac{\partial(k\bar{u}_i)}{\partial x_i}=\frac{\partial}{\partial x_j}(\Gamma_k\frac{\partial k}{\partial x_j})+G_k-Y_k\,, \tag{13}$$

$$\rho\frac{\partial(\omega\bar{u}_i)}{\partial x_i}=\frac{\partial}{\partial x_j}(\Gamma_\omega\frac{\partial \omega}{\partial x_j})+G_\omega-Y_\omega+D_\omega\,, \tag{14}$$

where k represents turbulent flow energy; ω represents turbulence frequency; Γ_k represents the dissipating rate of k ; Γ_ω is the dissipating rate of ω; G_k and G_ω are a turbulence generation term; Y_k and Y_ω are the turbulence dissipating term; D_ω represents the cross- dissipating term.

2.3. Geometry model and boundary conditions

The geometric information about the tunnel-embankment-train model and the settings of the boundary condition are given in Fig. 1. Using the CRH380B train as the research object, in order to facilitate modeling and mesh generation, the bogies,

pantographs and other components are ignored, and the train is only composed of three carriages. The actual length of the three carriages is 25.85 m, 24.83 m and 25.85 m, respectively. The actual width and height of the three carriages are 3.27 m and 3.89 m, respectively. The corresponding length, width and height of the head train are expressed in dimensionless forms such as *L*, *W* and *H*. In the numerical model, train A is located on the windward side track and moves in the positive direction of *X*; train B is located on the leeward side track and moves in the negative direction of *X*; trains A and B both run at speeds of 350 km/h. Under the action of the wind phase, the rain phase not only has a vertical falling velocity but also has a horizontal velocity along the incoming flow's direction (U_{if}). The overall width of the calculation domain is set to 54.7 *W* to guarantee that the rain phase can impact the train's windward side. The length and height of the calculated domain are 13.1 *L* and 10.3 *H*, respectively, and the specific geometric parameters of the embankment are shown in Fig. 1(b). The side surface for simulating incoming flow and the top surface of the computational domain in Fig. 1(c) are set to Velocity-inlet boundary conditions to control the wind and rain phases; the ground, embankment, train wall, and tunnel wall are used. No-slip Wall boundary conditions and other computational domain boundary conditions are set to Pressure-outlet.

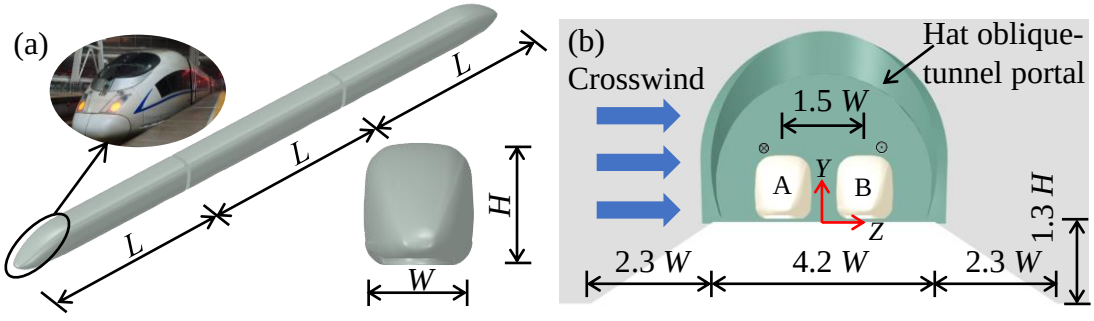

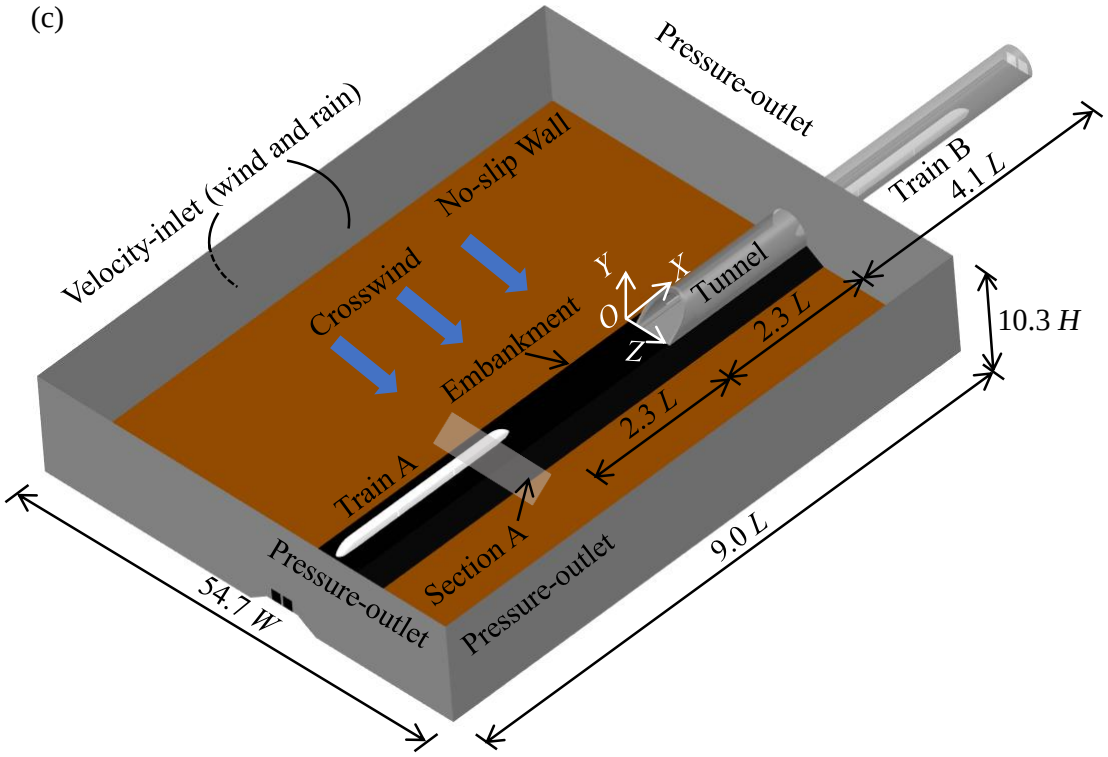

Fig. 1. Information about the geometric model: (a) the simplified train model; (b) Section A in Fig.1(c); (c) calculate domain and boundary conditions.

2.4. Grid method

The specific mesh details of the numerical model are shown in Fig. 2. The dynamic grid method used to realize the meeting of two trains at the tunnel entrance under a wind and rain environment is adopted in this paper. Yang et al., 2022b provides a detailed description of the moving grid approach. The information transmission through Interface is realized by the dynamic grid and the surrounding static grid region. Taking into account the intricate alterations to the flow field at the tunnel's entrance during the meeting, the grid refined area is set around it. The refined area's grid size is restricted to no more than 4×10^{-3} L, and the range size is 2.3 L×5.7 W×2.3 H. The spatial distribution of the two phases around the train is one of our concerns, so the grid area around trains needs to be further refined to meet the requirements of the turbulence model. In this paper, the surface of the train and tunnel

adopts a polygonal grid with a grid size of 8×10^{-4} and 1×10^{-3} L, respectively. A ten-layer boundary layer grid is set on the train wall, with a first grid thickness of 8×10^{-4} L (the value of y+ is close 30), and the growth rate is 1.2. The total mesh of the model is 42 million cells, and the SST k-ω model in Fluent software is employed for transient solving. The solution mode uses the second order, with a time step of 0.001 s (Courant number less than 1). The computing device is a supercomputer with a 120-core processor for a week's calculations.

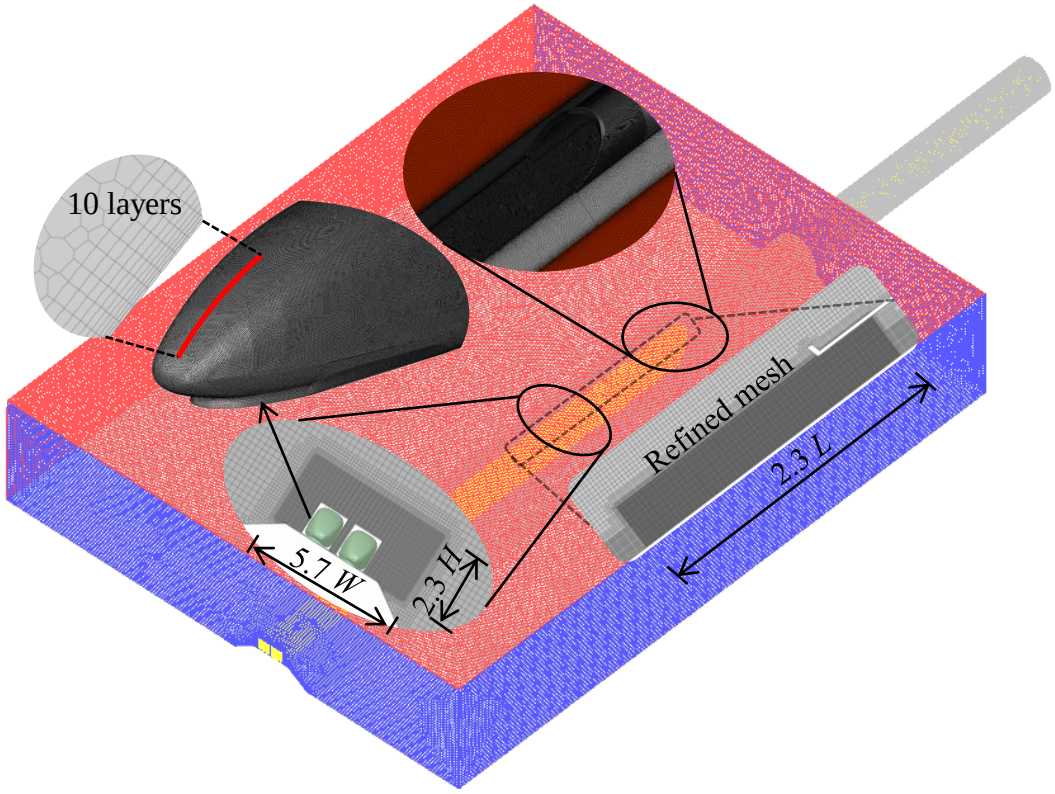

Fig. 2. Overview of the grid.

2.5. Model validation

2.5.1. Grid independence validation

In the numerical model, the setting scheme of grid size at different locations is related to the accuracy of the train's aerodynamic loads. A crucial part of the entire calculation process is played by the static grid refined area of the tunnel entry and the

dynamic grid refined area surrounding the train. Three boundary layer schemes are shown in Fig. 3(a), with total grid quantities of 34, 42 and 50 million, respectively. Taking a wind speed of 20 m/s and rainfall intensity of 0 mm/h (U_{if20} and I_0) and a wind speed of 30 m/s and 400 mm/h (U_{if30} and I_{400}) as examples, Figs. 3(b) and (c) show the rolling moment's time history curves corresponding to the three grid schemes. As can be seen, a change in the number of boundary layers has a significant influence on the value but has little effect on the train's rolling moment change law in Fig. 3(b) and (c), and the main impact area is in the embankment and the tunnel entrance sections. In U_{if20} and I_0 and U_{if30} and I_{400}, the difference in magnitude between scenarios 1 and 2 is 7.6% and 17.9%. Compared with scheme 1, the amplitude of the rolling moment of scheme 2 and scheme 3 is closer; the difference is only 3.3% and 2.5%, but the calculation time and data file storage space of scheme 3 are basically 1.5 times that of scheme 2. Therefore, schemes 1 and 3 are discarded due to their poor calculation accuracy and computational efficiency, respectively, and the scheme of 10 boundary layers is selected.

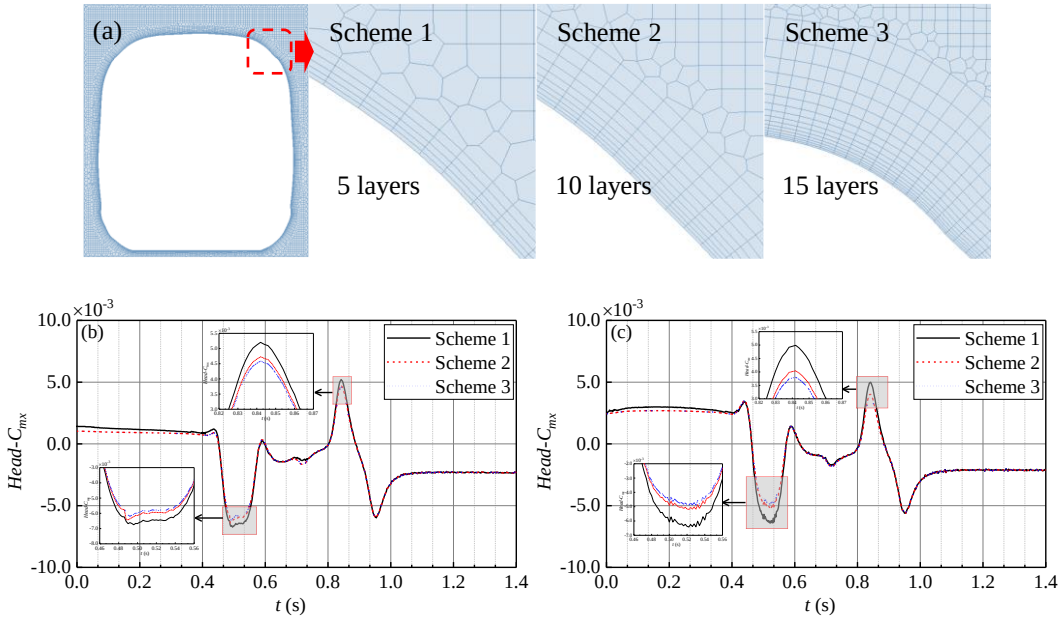

Fig. 3. Grid independence validation: (a) schemes about the boundary layer number;

(b) rolling moment in U_{if20} and I_0; (c) rolling moment in U_{if30} and I_{400}.

2.5.2. Validation of two trains meeting

The aerodynamic loads of the carriage will change drastically due to the head wave and wake wave during the meeting of the two trains. The sudden peak of the aerodynamic loads is directly related to the degree of deterioration of the aerodynamic performance during the meeting. As a result, it is necessary to compare the turbulence model and associated boundary setting scheme used in this study with a wind tunnel test involving two trains colliding. The wind tunnel test (Hu et al., 2022) is given in Fig. 4(a), and the train is a 1:20 scale model. The wind velocity is 8 m/s, the train velocity is 5.6 m/s, and the two trains are meeting at the bridge. Since the train model goes through the acceleration, constant speed and deceleration stages, respectively. The speed of the acceleration and deceleration stages is unstable, and the aerodynamic coefficient is subject to many uncontrollable factors. Therefore, only the train's aerodynamic coefficient in the stable section is verified. A numerical model is built with reference to the wind tunnel test, and boundary condition type and the turbulence model used are consistent with the working conditions in this paper. From the analysis of Fig. 4(c), the results obtained by the numerical model and the wind tunnel test have a great agreement. The amplitude errors of the C_z and C_{mx} are 6.9% and 4.5%, respectively. Fluctuations in vehicle speed during the test and interference from some factors, such as surface roughness of numerical models and scaled models, may be the main reasons for the difference in results. Hence, the dynamic mesh simulation scheme adopted in this paper can be considered reasonable.

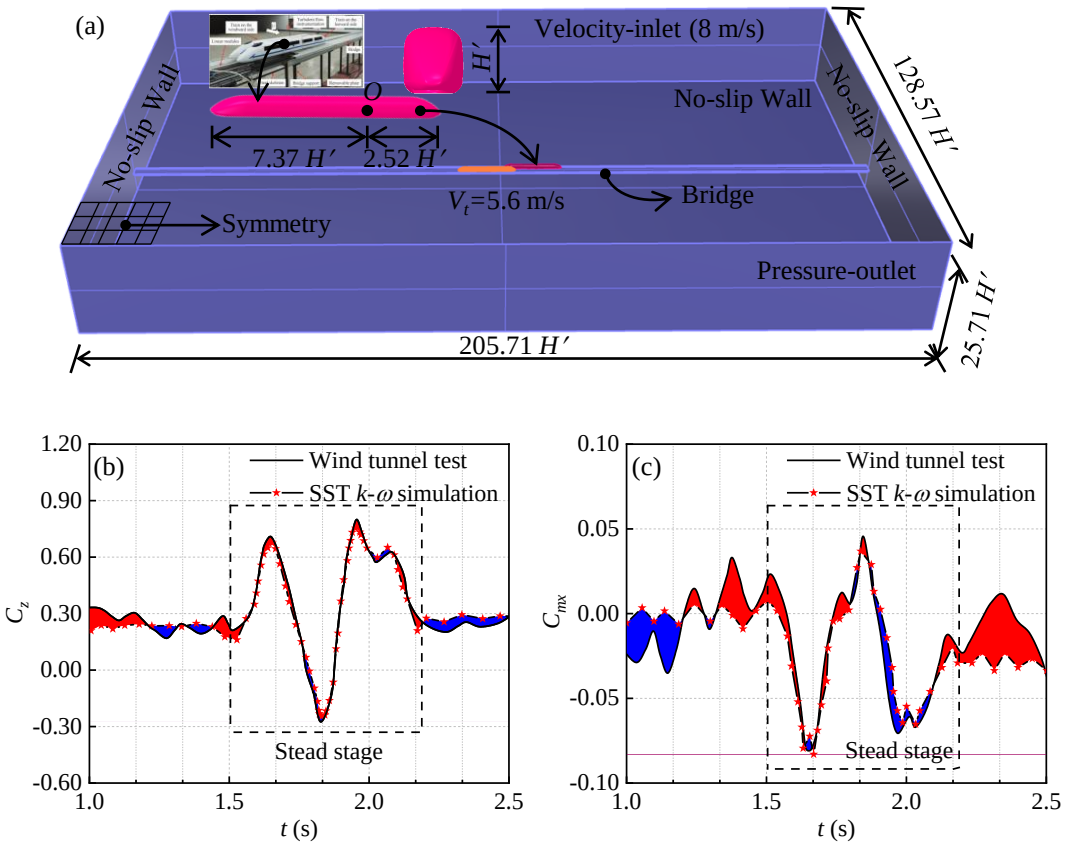

Fig. 4. Validation of two trains meeting: (a) calculate domain and train model; (b) lateral force coefficient; (c) rolling moment coefficient.

2.6. Introduction of working conditions and data processing

In order to analyze the of train's aerodynamic performance during meeting under different rainfall intensity and wind speed conditions and reveal the spatial distribution law and evolution mechanism of the rain phase during under correspond conditions. The combination of three wind speed classes (20, 25 and 30 m/s) and five rainfall intensity classes (0, 100, 200, 300 and 400 mm/h) is considered, and six different calculation scenarios are listed in Table 1 for analysis. The analysis focused on train A, which enters the tunnel from outside the tunnel on the windward line. Train B exits the tunnel from the leeward line. Four feature positions are chosen for analysis to help with the comparison of flow field differences between various working conditions. The feature position is selected based on the distance between the

train A's nose tip and the tunnel entrance, which is X=-1 L, X=0 L, X=1.5 L and X=3 L, respectively. The wind-rain load time history curves are obtained by a User-defined Function (Yang et al., 2022b). This paper focuses on the analysis of the lift, lateral forces, rolling, yawing and pitching moments, which are dimensionless according to the specification (BS EN, 2006), and the specific treatment formula is shown in Yang et al. (2022b).

Table 1 Introduction to working condition parameters.

Cases	Schemes	Speed of train	Speed of incoming flow	Rainfall intensity
U_{if20} and I_0	Wind	350 km/h	20 m/s	0 mm/h
U_{if20} and I_{200}	Wind and rain	350 km/h	20 m/s	200 mm/h
U_{if20} and I_{300}	Wind and rain	350 km/h	20 m/s	300 mm/h
U_{if20} and I_{400}	Wind and rain	350 km/h	20 m/s	400 mm/h
U_{if25} and I_{400}	Wind and rain	350 km/h	25 m/s	400 mm/h
U_{if30} and I_{400}	Wind and rain	350 km/h	30 m/s	400 mm/h

3. Results and analysis

3.1. Wind-rain loads

The three carriages' wind-rain loads under four conditions are shown in Fig. 5, and the analysis of wind-rain loads is helpful to master the stress state of the train in the whole process of operation so as to design the wind-resistant structure. Three feature positions have been marked in the Fig. 5 with black lines for ease of analysis. The entire calculation process can be divided into three stages. The first stage is for train A to run alone on the embankment (X<0 L). The second stage is for train A to meet at the entrance of the tunnel (0 L<X<3.0 L). The third stage is for train A to fully enter the tunnel (X>3.0 L). In the first stage, the focus is on the effect of rain on the train's average aerodynamic loads. In the second stage, the focus is on the influence of I and U_{if} on the amplitude of aerodynamic loads during two trains meeting. In order to eliminate the fluctuation of single time-node data and the influence of the acceleration effect on trains at tunnel entrance and to achieve the research objectives of the first stage, the average aerodynamic loads of train A at 0-0.2 s are selected for comparison. In order to quantitatively compare the difference in the train's wind-rain load

amplitudes between different cases and analyze its relationship with rainfall intensity, the amplitude of wind-rain load coefficient (ΔC) is introduced in Eq. 15, and the value range is 0.2-1.4 s.

$$\Delta C = C_{\max} - C_{\min}, \tag{15}$$

where, $C_{\max}$ and $C_{\min}$ represents the positive and negative peak values of the wind-rain loads. Fig. 6 shows the normalization results of the train's ΔC, and the working condition with a wind speed of 20 m/s and a rainfall intensity of 400 mm/h is used as the reference working condition. Table 2 shows the average wind-rain load coefficients under U_{if20} and I_0 and U_{if20} and I_{400} when train A runs alone on the embankment section.

Based on the analysis of Fig. 5, Fig. 6 and Table 2, it can be seen that the variation rule of the wind-rain load coefficients is basically consistent in the four working conditions. In the early stages of the first phase, the train is subjected to a steady wind or wind-rain load. In the late stage of the first stage, only the head train is affected by the acceleration effect from crosswinds near the tunnel entrance, and the C_y, C_z and C_{mz} of the lead train increased by 67.7%, 6.9% and 13.3%, respectively. In the second stage, the train is mainly affected by the pulsating impact generated by the meeting. In the third stage, the loads of the train are basically equal because it completely driven into the tunnel and not affected by the meeting. This is followed by a detailed analysis of the first and second phases, respectively.

In the first stage, the average wind-rain loads of the trains in U_{if20} and I_{400} are higher than those of U_{if20} and I_0 (except for the tail train's lateral force and the middle train's rolling moment), and the influence degree from rain phase on different carriages is significantly different in Fig. 5. This shows that under the action of wind-rain, the rain has an impact force on the train's surface. Under the same wind speed,

the rain phase has an additional contribution to the aerodynamic loads on the train body. In addition, the rain phase exhibits different aerodynamic effects due to the difference in the flow field around different carriages. The $\overline{C}_z$, $\overline{C}_{my}$ and $\overline{C}_{mz}$ of the head train in the U_{if20} and I_{400} are higher than those of the middle and tail trains. For example, the $\overline{C}_z$ of the head train is about three times that of the middle train, and the $\overline{C}_{my}$ is about two times that of the tail train. This indicates that the lateral swing, serpentine movement and pitching motion posture of the head train are more complex than those of the middle and tail trains under the influence of wind-rain, which is basically consistent with the research conclusion under pure crosswinds (Ouyang et al., 2023). For the head train, the degree of influence of rain on various load indicators also differs. The effect of rain on the head train's $\overline{C}_z$ and $\overline{C}_{mx}$ is small, and the $\overline{C}_z$ only increased by 2.12%. However, the $\overline{C}_y$, $\overline{C}_{my}$ and $\overline{C}_{mz}$ of the head train can be increased by 6.25%, 9.68% and 10.31%, respectively. This indicates that the impact of rain phase on the lateral force is weaker than that of rain phase on the flow field around the roof. There are two reasons for this difference may be that the water film attached to the roof of the train increases the flow velocity, leading to the increase of lift and yaw moment, while the rain phase leads to the increase of negative pressure on the leeside of the train, leading to the increase of lateral force. It also shows that it is unreasonable to consider only the wind load when analyzing the dynamic response index of the train and the driving safety under wind-rain conditions, and the rain load on the train must also be considered.

In the second stage, the influence of the rain phase on the amplitude of the wind-rain load is first analyzed. It can be seen from the time history curve that during the meeting at the tunnel entrance, the mutual aerodynamic impact generated by the relative movement of the two trains dominates the wind-rain forces of the carriage,

and the rain phase has the amplification effect relative to part of the wind-rain loads, but it is obviously weaker than the influence of wind speed. The impact of rain on ΔC_y and ΔC_z is limited, and the corresponding difference does not exceed 5%. The ΔC_{mz} of the head, middle and tail trains under the U_{if20} and I_{400} are 10.7%, 10.1% and 13.7% higher than those under the U_{if20} and I_0, respectively. It is worth noting that when the train is in a critical wind speed environment, the amplification effect of rain on aerodynamic loads may cause the train's dynamic response index to exceed the limit, which needs the attention of researchers. Additionally, the track surface will appear both dry and wet states for the tunnel shielding, and the wheel-rail will experience dry and wet contact conversion during the vehicle's entry and exit from the tunnel. This could further exacerbate the deterioration of the wheel-rail relationship and result in the train derailing (Chen et al., 2020; Wu et al., 2022).

Next, the relationship between the wind-rain load amplitudes of the three carriages and the U_{if} is analyzed under the condition of a constant rain phase. The aerodynamic amplitudes of the three carriages are basically positively correlated with the U_{if}. This is because the influence of crosswind speed on aerodynamic amplitude dominates throughout operation. It is worth noting that in the head and tail trains, the ΔC_{mx} is negatively correlated with the U_{if}, while the ΔC_{mx} of the middle train has no obvious linear relationship with the U_{if}. This is because wind speed not only increases the rolling moment value of the train before the meeting, but also changes the pulse peak generated by the train during the meeting, which leads to the fact that the amplitude of the rolling moment of different carriages is not significantly related to the change in wind speed.

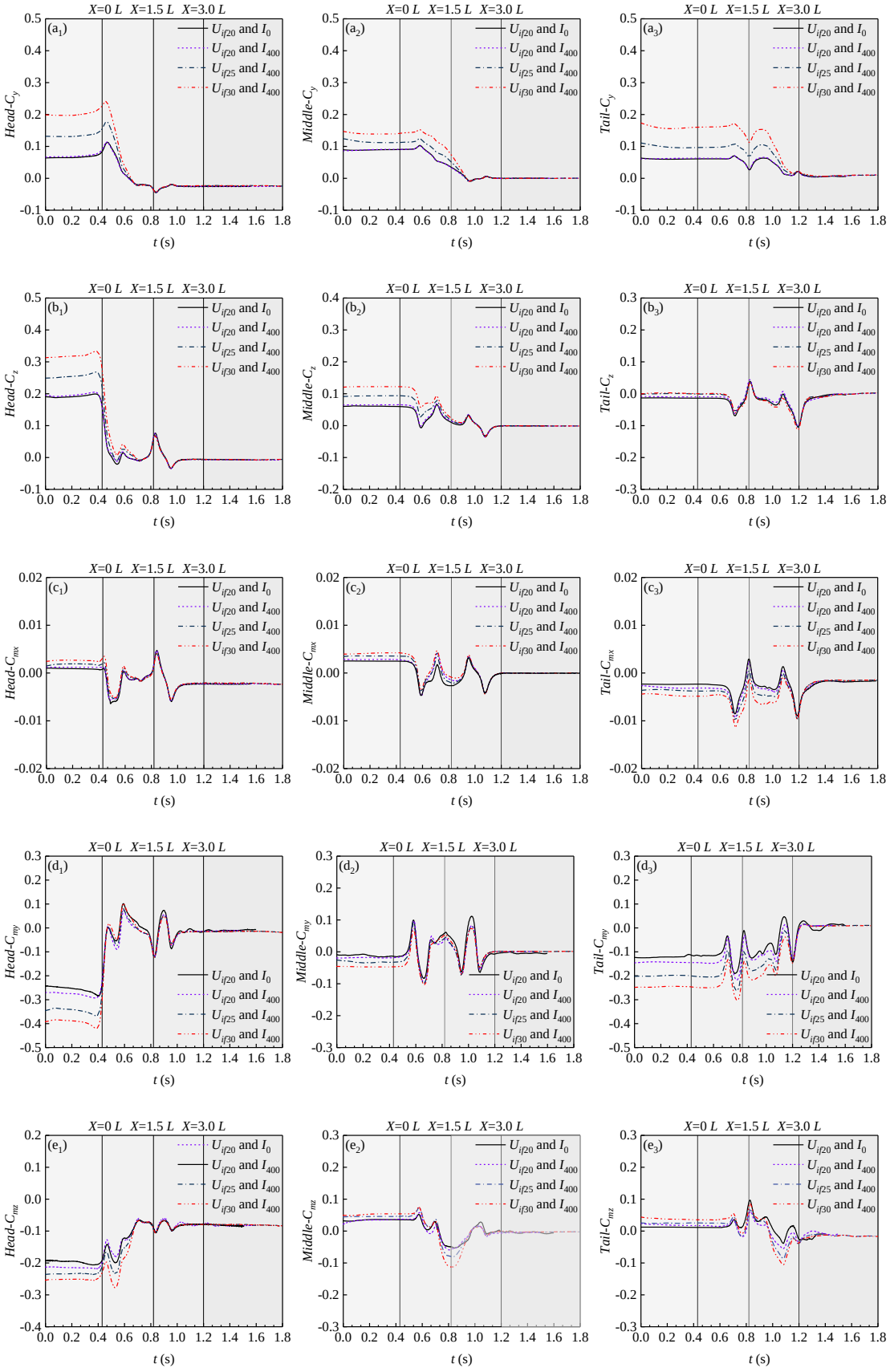

Fig. 5. Time history curve of wind-rain loads of the train under different conditions: (a-e) represent the C_y, C_z, C_{mx}, C_{my} and C_{mz}, respectively. Subscripts 1, 2 and 3

represent the corresponding head, middle and tail trains, respectively.

Table 2 Comparison of wind-rain load coefficients under U_{if20} and I_0 and U_{if20} and I_{400}.

	U_{if20} and I_0			U_{if20} and I_{400}		
	Head train	Middle train	Tail train	Head train	Middle train	Tail train
$\lvert\bar{C}_y\rvert$	0.064	0.088	0.061	0.068(6.25%)	0.088(0.00%)	0.061(0.00%)
$\lvert\bar{C}_z\rvert$	0.189	0.061	0.013	0.193(2.12%)	0.065(6.56%)	0.009(-30.77%)
$\lvert\bar{C}_{mx}\rvert$	0.001	0.003	0.002	0.001(0.00%)	0.004(33.33%)	0.003(50.00%)
$\lvert\bar{C}_{my}\rvert$	0.248	0.010	0.124	0.272(9.68%)	0.019(90.00%)	0.143(15.32%)
$\lvert\bar{C}_{mz}\rvert$	0.194	0.033	0.012	0.214(10.31%)	0.031(-6.06%)	0.021(75.00%)

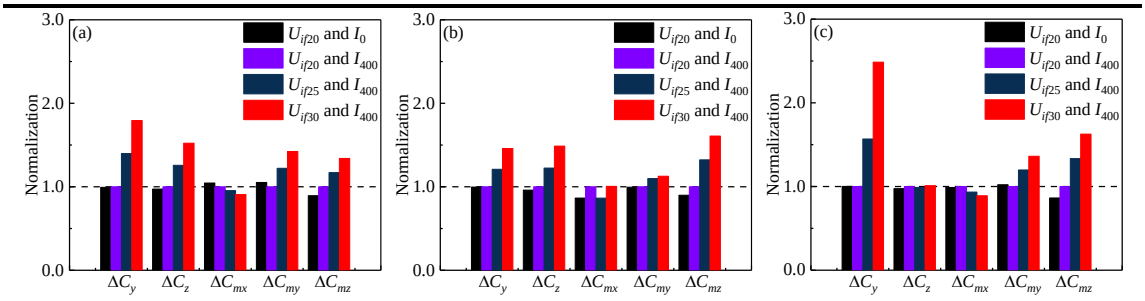

Fig. 6. Normalized wind-rain loads amplitude: (a) head train; (b) middle train; (c) tail train.

3.2. Characteristic surface of the wind-rain loads

To further analyze the impact of rainfall intensity and wind speed on the $\bar{C}$ and ΔC of the train in the first and second stages. Considering that during the entire operation, the wind-rain load of the head train is generally higher than those of the middle and tail trains. Fig. 7 shows the average wind-rain loads and its amplitude characteristic surfaces of the head train at wind speeds of 20 m/s, 25 m/s and 30 m/s, respectively, when the rainfall intensity is 0, 100, 200, 300 and 400 mm/h, respectively. The feature surface is fitted using a 3D plane equation ($z = a + bI + cU_{if}$), and when the coefficients *b* and *c* are positive or negative, it means that the wind-rain loads are positively or negatively related to *I* and U_{if}, respectively. The magnitudes of *b* and *c* represent the strength of the wind-rain loads affected by rainfall intensity and wind speed. The gray lines in the figure represent contour lines. Based on this, the wind-rain characteristic surface given in Fig. 7 can provide a reference value for

engineering builders and subsequent researchers who study wind-rain loads.

According to the analysis of Fig. 7, the average wind-rain loads and their amplitude have a significant linear correlation with U_{if} and I. Analyzing the relationship between wind-rain loads (including average value and amplitude) and rainfall intensity, it can be seen that the average wind-rain loads are positively correlated with rainfall intensity because the increase in the volume fraction of the rain phase leads to an increase in the impact of the wind-rain loads on the train. ΔC_y, ΔC_z, ΔC_{mz} are positively correlated with rainfall intensity, while ΔC_{mx} and ΔC_{my} are negatively correlated with rainfall intensity, which may be due to the influence of the water film attached to the train body on the pulse force generated during the meeting. It is worth noting that with the increase in rainfall intensity, the average wind-rain moments are faster than the change rate of wind-rain forces, and the change rate of $\overline{C}_{my}$ reaches 2.3 times that of $\overline{C}_{z}$, and the change rate of $\overline{C}_{mz}$ reaches 4.9 times that of $\overline{C}_{y}$; the amplitude of wind-rain loads also shows this phenomenon, and the change rate of ΔC_{mz} reaches 4.8 times that of ΔC_{y}. This shows that the rain phase has a higher degree of deterioration than the yawing and pitching attitude of the train when running on the embankment and the pitching attitude at the meeting. As the intensity of rainfall increases, wind-rain moments deserve more attention than wind-rain forces. Analyzing the relationship between wind-rain loads (including average value and amplitude) and wind speed, it can be seen that the average wind-rain loads and its amplitude are positively correlated with wind speed (except for ΔC_{mx}). It is worth noting that as wind speed increases, the change rate of the average wind-rain forces is higher than that of the wind-rain moments; the change rate of $\overline{C}_{y}$ reaches 3.4 times that of $\overline{C}_{mz}$; a similar phenomenon is not found in the change law of the amplitude of the wind-rain loads and wind speed, which may be caused by the influence of the

meeting. Finally, comparing the influence of U_{if} and I on wind-rain loads (including average value and amplitude), it can be seen that the average wind-rain loads and their amplitude are significantly more affected by wind speed than rainfall intensity. For example, for the average lift force and its amplitude, c is 1248.8 and 1420.9 times that of b, respectively. This is mainly because the volume fraction of the rain phase is small, and the increase in I has a weak effect on the aerodynamic loads of the train compared to the increase in U_{if}.

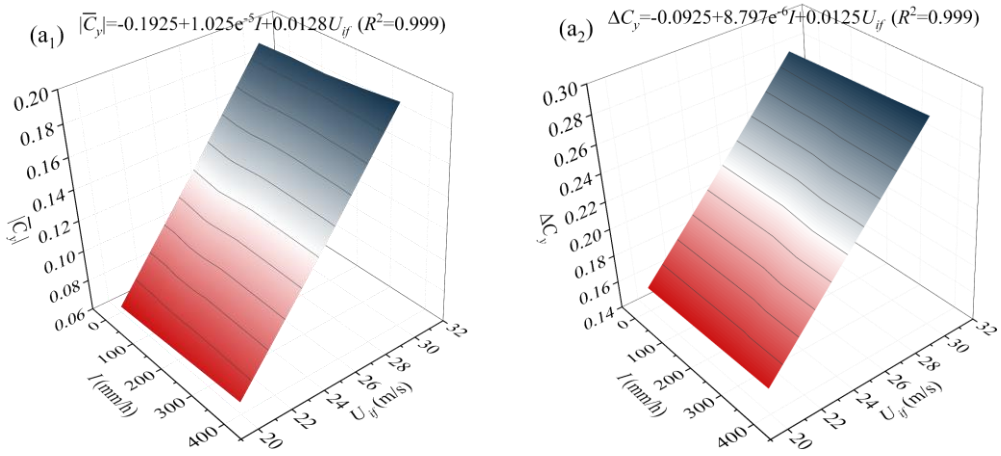

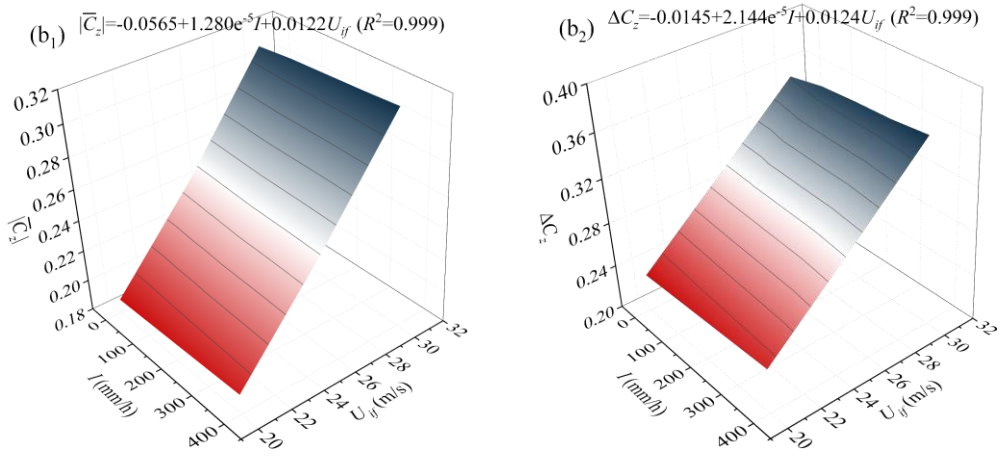

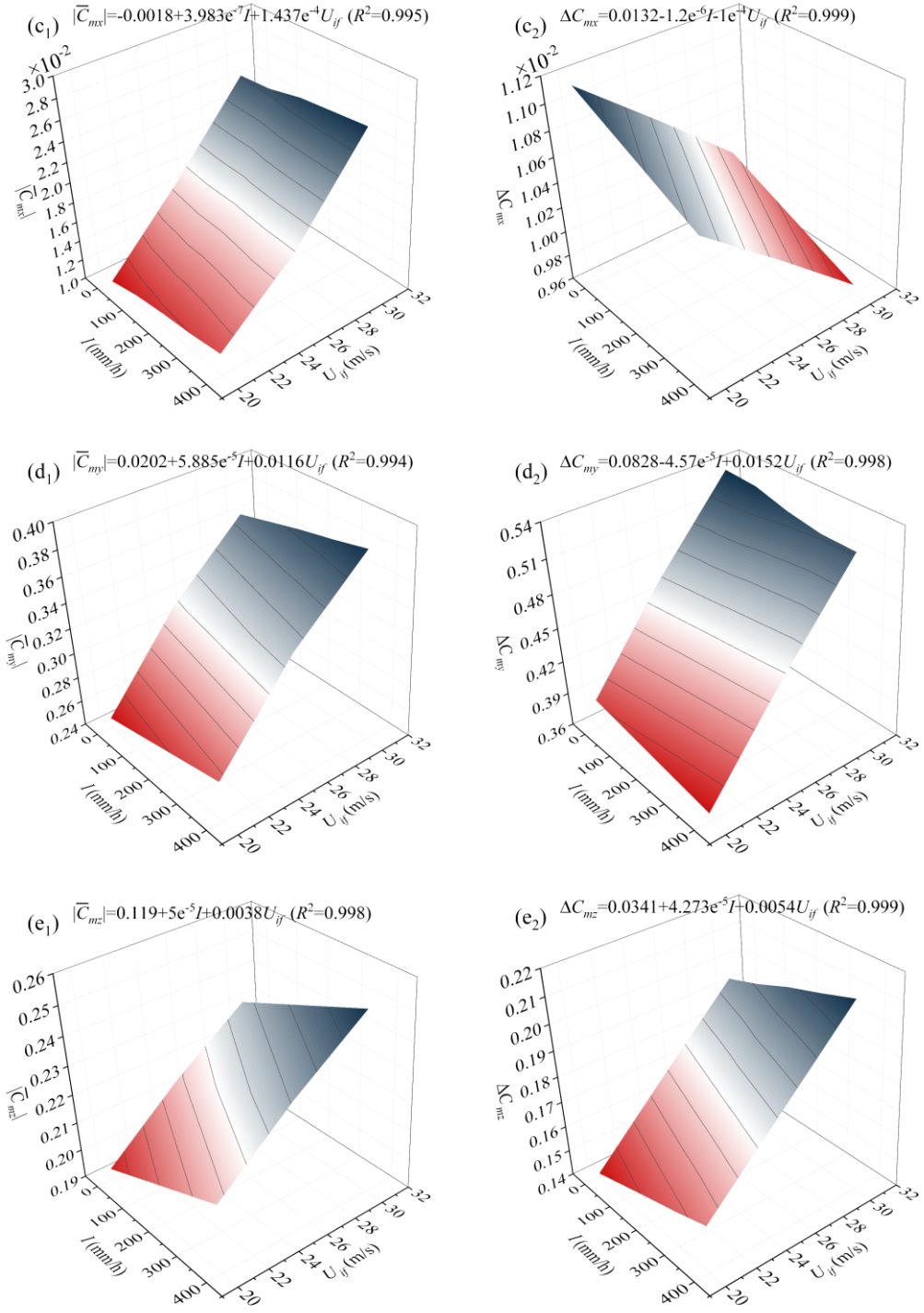

Fig. 7. Characteristic surface of the wind-rain loads (including average value and amplitude) with wind speed and rainfall intensity: (a-e) represent the C_y, C_z, C_{mx}, C_{my} and C_{mz} of the head train, respectively. Subscript 1 and 2 represent before and during the meeting, respectively.

4. Discussion about the flow field mechanism

4.1. One train running on the embankment

4.1.1. Distribution of pressure coefficient

The distribution of pressure is an aspect that reflects the train's aerodynamic performance. In the second stage, the wind-rain force of the carriage is mainly dominated by the pulsating impact of the train, so the pressure coefficient at a single moment in this stage is not suitable for analyzing the difference between working conditions. In the first stage, the wind-rain loads of the train are basically stable with time, and the distribution law of the pressure coefficient is basically stable, which can help better analyze the difference between different cases. Therefore, the pressure coefficients of the horizontal plane and the cross section at the time of t=0.2 s are used as representatives to compare the difference in the distribution of pressure coefficients between different cases. The horizontal distribution of pressure coefficients in U_{if20} and I_0, U_{if20} and I_{400}, U_{if25} and I_{400} and U_{if30} and I_{400} is shown in Fig. 8 in order to analyze the influence of the rain phase on the pressure coefficient and its distribution law with the U_{if} under wind-rain environments. The horizontal contour line is 0.5 H from the underbody, starting from the tail train's nose tip (O_1), passing through the windward side body to the head train' nose tip (O_2) and then returning to the O_1 through the leeward side body. The pressure coefficient's cross-sectional distribution in the four cases is shown in Fig. 9, and subscript 1, 2, 3 corresponds to sections S1, S2 and S3, respectively. Each carriage set three cross-sections, and the cross-sections of the head train are named H-S1, H-S2, H-S3 respectively; the cross-sections of the middle train are named M-S1, M-S2, M-S3; the cross-sections of the tail train are named T-S1, T-S2, and T-S3, and the specific location of the cross-section is shown in Fig. 9. The calculation formula of pressure coefficient is showed in Eq. 16.

$$C_p = \frac{P_{face} - P_0}{0.5\rho V_a^2}, \tag{16}$$

where C_p represents the pressure coefficient, P_{face} represents the pressure of the train wall, P_0 represents the reference pressure in the calculation domain, ρ represents the air density, V_a represents the couple velocity between the train and incoming flow.

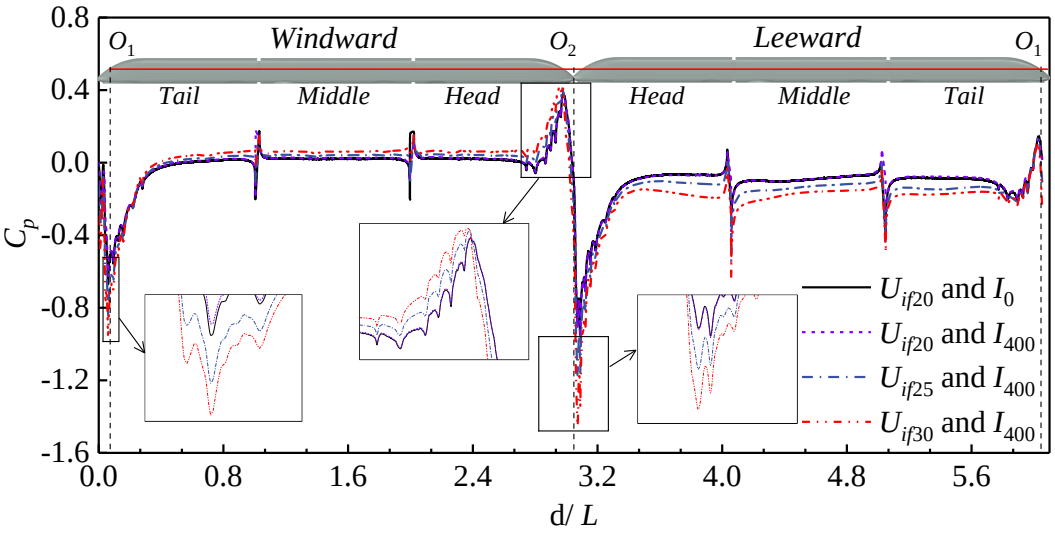

Fig. 8. Horizontal distribution of pressure coefficient around the train A.

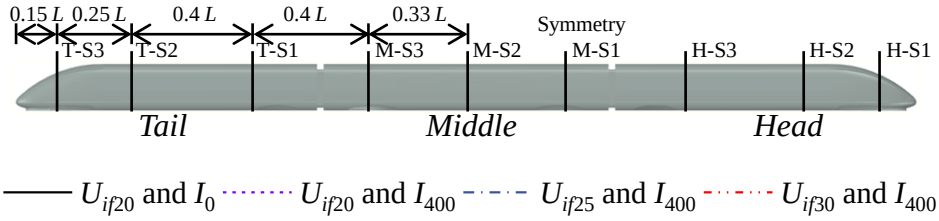

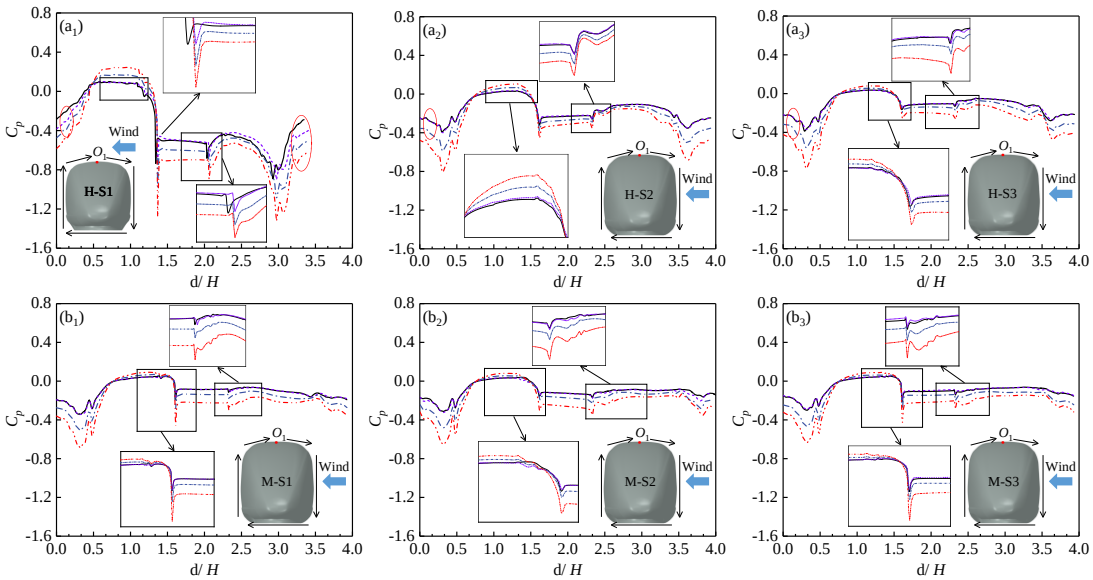

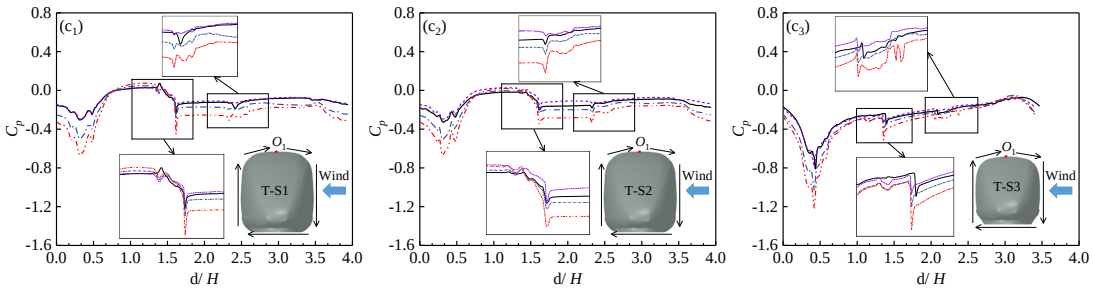

Fig. 9. Cross-sectional distribution of pressure coefficient around the train A: (a) head train of the train A; (b) middle train of the train A; (c) tail train of the train A. Subscript 1, 2 and 3 represent the S1, S2 and S3 slices of the corresponding carriages, respectively.

As can be seen from the analysis in Fig. 8, the difference between the with or without rain phase is mainly reflected in the head and tail train's nose tips, while there is no significant difference in the constant section body. Under rainy conditions, the positive and negative pressure at the head train's nose tip is about 2% higher than that pure crosswind, and the positive and negative pressure at the tail train's nose tip is about 12.5% and 6% lower than that of pure crosswinds. This reason is mainly because the windward side of the head train's nose tip is affected by the impact of the rain phase and the pressure increases, and the negative pressure on the leeward side increases due to the around flow's acceleration. But, the development of the vortex structure is interfered with by the rain phase around the tail train's nose tip. This further explains the effect of the rain on the head and tail train's lateral forces in Fig. 5. When the wind speed changes, the windward side's pressure coefficient distribution is close, and the leeward side's pressure coefficient distribution is quite different. This is caused by the acceleration of the incoming flow through the train body and the instability of the vortex structure that is constantly evolving on the train body's leeward side. This is also the primary cause of the small difference in the positive pressure region in the ring pressure coefficient in Fig. 9, and the large difference in

the negative pressure region.

In the cross-sectional distribution of the pressure coefficient, the difference in rain phase is mainly reflected in H-S1 and T-S2, and there is no significant difference in other cross-sectional positions. For example, in the H-S1 section, the head train's windward roof can be found to be 38.8% greater in rainy conditions than in a pure crosswind. This difference gradually disappeared as the contour line reaches the windward side, and no significant differences caused by the rain phase are found on the train's windward side or the underside, but the difference in the rain phase reappeared on the train's leeward side. This indicates that the rain phase affects the flow around the roof at the variable section and the strength of the vortex structure corresponding to the leeward side. Further explanation is as follows: the rain phase causes the roof to accelerate around the flow, and then the negative pressure increases, and the lift force increases; considering the lateral impact effect of rain phase, it is finally manifested as the phenomenon of increased lateral force. In addition, it can be found that the degree of pressure coefficient fluctuation at the variable section of the head and tail trains in these four cases is significantly more severe than that at the equal section, mainly because the variable section not only has accelerated around flow but also has uneven shear of the longitudinal velocity of the fluid caused by longitudinal geometric asymmetry. This shows that the head and tail trains' aerodynamic performance is more susceptible to wind-rain deterioration than the middle train, especially the variable section. Except for the head and tail trains' variable sections, the difference on the windward side' pressure coefficient of other sections decreases as wind speed increases, whereas it increases on the underbody, leeward side and roof. This demonstrates that as wind speed increases, the winding of the roof and the development and shedding of the train's leeward vortex structure

become more important in the study of the train's aerodynamic performance.

4.1.2. Spatial distribution of rain phase

In order to analyze the spatial distribution differences of rain phase under different rainfall intensities and wind speeds, Fig. 10 shows the rain phase's volume fraction around the train under the cases in Table 1 at the time of t=0.2 s. Since the rain phase is not added to U_{if20} and I_0, it is not considered in Fig. 10. Each case uses three slices, located in the middle of the three carriages.

According to the analysis of Fig. 10, the spatial distribution difference of the rain phase between various cases is primarily represented in the head train's leeward side, with no significant difference between the middle and tail train. For middle and tail trains, when the wind speed is constant and the rainfall intensity increases, there is no significant difference in the distribution of rain phase. When the rainfall intensity remained constant and the wind speed increases, the spatial distribution area of the rain phase on the leeward side of the roof gradually increases. Furthermore, in the same case, the head train's leeward side has a higher rain phase volume fraction than the middle and tail trains. This reveals the reason for the difference in the distinction of the head train's pressure coefficient caused by the rain phase in Section 4.1.1. To facilitate analysis, the head train's leeward area is simply divided into four zones (z1, z2, z3 and z4) according to the difference in volume fraction. Among them, the z1 area is close to the leeward side wall of the train, and its volume fraction is at least close to 0 due to the blocking of the train body and the carrying effect of the wind on the rain phase; z2 is the area with the highest volume fraction of the rain phase on the train's leeward side, which is greatly affected by rainfall intensity and wind speed. An interesting phenomenon occurs in area z3; that is, although the height of z3 is close to the roof of the train, its volume fraction is smaller than that of areas z2 and z4 on both

sides. The reason for this phenomenon may be that: because the density of the rain phase is much higher than that of the air, after the incoming flow bypasses the roof, the rain phase is affected by gravity and moves downward, and the wind phase maintains the original movement trend, which in turn leads to the diversion phenomenon between the rain and wind phases. z4 region represents the volume fraction in the domain environment, which is mainly affected by the intensity of rainfall. Under the condition of constant wind speed, the slope of the dividing line of z2 and z3 is roughly the same, while the slope of the dividing line of z2 and z3 gradually decreases under the condition of increasing wind speed. It can be speculated that the slope of the dividing line between z2 and z3 has a high correlation with the incoming wind speed. The red area in the z2 region expands with the increase of I, while the area in the z1 region is continuously compressed. This means that the influence range and intensity of rain relative to the flow field on the leeside of the train increase, which is also the reason why the lateral force of the train increases with the intensity of rain. With an increase in wind speed and constant volume of rain phase, the area of z1 continues to grow, the area of z2 continues to decrease and gradually moves towards the roof, and z3 gradually moves away from the train and downstream. Since the volume fraction of rain phase in z1 region is almost 0 under these working conditions, it can be inferred that if the rainfall intensity is unchanged, the increase of wind speed will weaken the influence of rain on the flow field on the train's leeward side.

In order to reveal the mechanism of the influence of rain phase on the turbulent intensity of the wind phase, the cross-sectional slices in U_{if20} and I_0 and U_{if20} and I_{400} are shown in Fig. 11, and the slice position is the same as in Fig. 10, colored by turbulence intensity, which describes the fluctuation of wind speed. It is clear from the

analysis of Fig. 11 that the turbulence intensity is significantly influenced by the rain phase. First, the rain phase will increase the fluid's turbulence intensity on the head train's leeward side. For example, the red area on the head train's leeward side in U_{if20} and I_{400} is significantly larger than the corresponding position in U_{if20} and I_0, and this difference position corresponds to the region with a higher volume fraction of the rain phase in Fig. 10. The reason for this phenomenon may be that the rain phase is separated by gravity with the wind phase on the train's leeward side, which leads to a difference in flow velocity between the area with a high rain volume fraction and the area with a low rain volume fraction, thereby promoting the development of turbulence intensity. In addition, the water film adhering to the train body' surface also affects the flow speed of the wind phase around the train. The phenomenon of increasing turbulence intensity in the rain phase is also reflected in slices 2 and 3 in Fig. 11, while the turbulence intensity on the corresponding carriage's leeward side does not increase significantly. This is mainly because the rain phase near the middle and tail trains in the U_{if20} and I_{400} is mainly distributed in the roof position, while the rain phase's volume fraction in the corresponding leeward side position is almost 0.

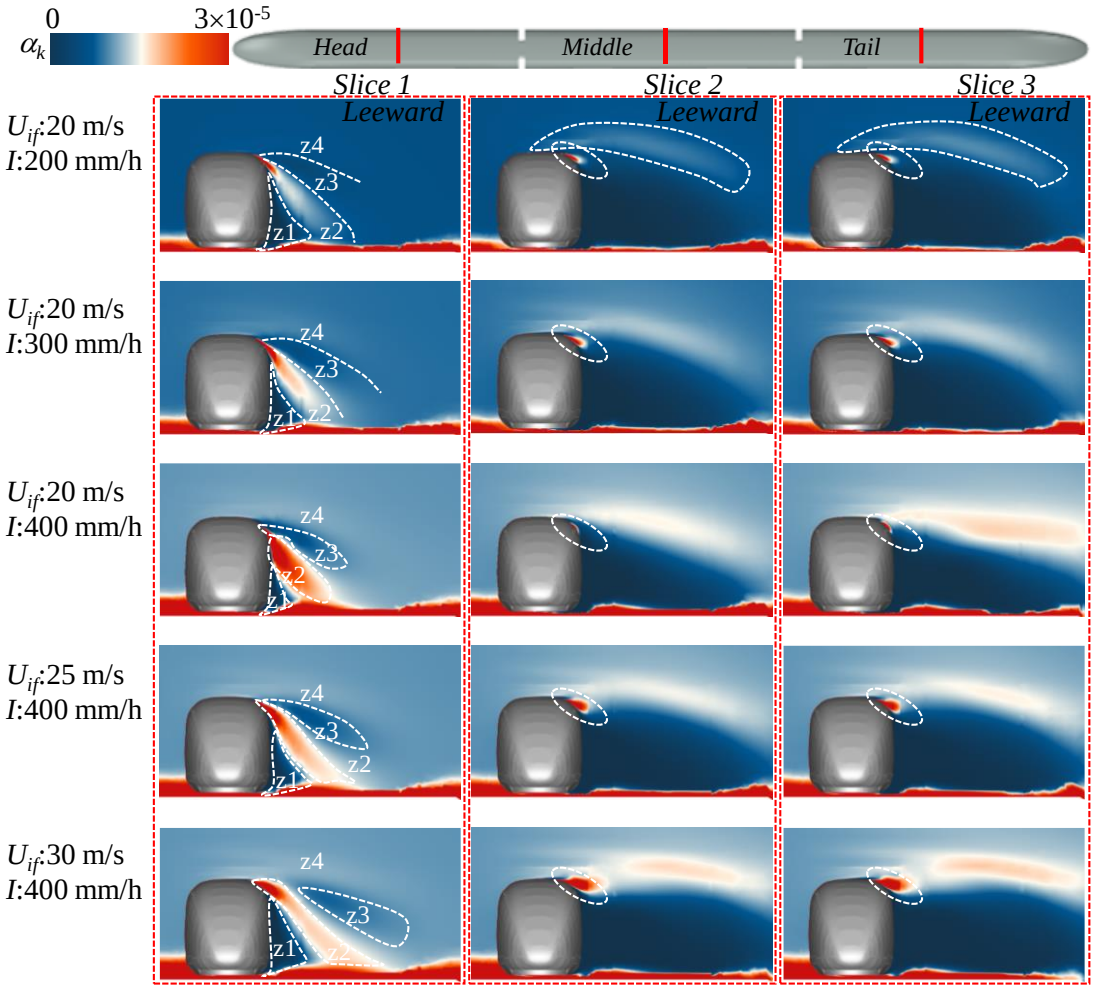

Fig. 10. Volume fraction distribution of rain phase at t=0.2 s.

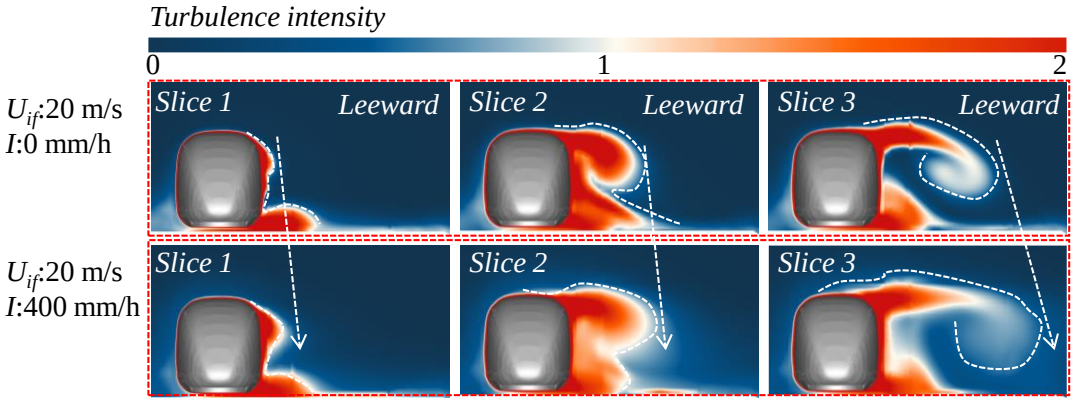

Fig. 11. Comparison of turbulence intensity with or without rain phase.

4.2. Evaluation of wind-rain field during the meeting

In order to reveal the spatiotemporal evolution mechanism of the wind-rain field during the meeting. Fig. 12 shows the horizontal pressure cloud around the train at

different characteristic locations in U_{if20} and I_0, U_{if20} and I_{400} and U_{if30} and I_{400}. Figs. 13 and 15 show the spatial transient distribution of pressure and rain phase at different carriage cross-sections at three feature positions, and the position of the carriage cross-section is consistent with the position of the section in Fig. 10. In the analysis process, the rainfall intensities of 0 mm/h and 400 mm/h are selected as representatives to analyze the difference in rain phase on the pressure field, and the incoming flow velocities of 20 m/s and 30 m/s are chosen to analyze the influence of wind velocity on the pressure field.

Based on the distribution characteristics of rain phase in Section 4.1, the train's leeward side is still the focus area. From the red oval area in Fig. 12(a), it can be seen that the leeward side's negative pressure of under the conditions of U_{if20} and I_{400} is higher than that of U_{if20} and I_0. The reason for this phenomenon may be that the rain phase sandwiched in the wind phase and the water film attached to the roof of the train cause the roof flow to accelerate, and the acceleration of the roof flow causes the train's leeward vortex structure to move away from the body and the negative pressure to increases. Therefore, compared with pure crosswinds, the pressure difference between the two sides of the train body under wind-rain conditions increases, and the lateral deflection attitude of the train body becomes more significant.

In addition, under the premise of unchanged rainfall intensity, the windward side's positive pressure and the leeward side's negative pressure gradually increase as the wind velocity increases, and the aerodynamic performance of the train body will further deteriorate. The phenomenon of an additional increase in negative pressure on the train's leeward side caused by wind-rain phases is also reflected in Fig. 12(b).

It is worth noting that this phenomenon gradually weakens as the train meeting

progresses. The cause of the wind-rain load fluctuation during the meeting can be found in the four different characteristic positions in Fig. 12. The pressure in the small gap between the two trains is essentially unaffected by the rain phase during the meeting, and the wind-rain loads are primarily controlled by pulsating impacts. The pulsating impacts comes from the head and wake waves of train B. The aerodynamic force of train A's head train stabilizes near zero as it enters the tunnel. Furthermore, as seen in the red elliptical region of Fig. 12(d), train A's wake vortex interacts with the flow field surrounding train B as it enters the tunnel. Under rainy conditions, rain phase will be carried into the wake vortex, and when the wake vortex of train A and the incoming flow are coupled, the volume fraction of the rain in the tail vortex may be much higher than the incoming flow, which might have a more significant impact on train B's aerodynamic efficiency.

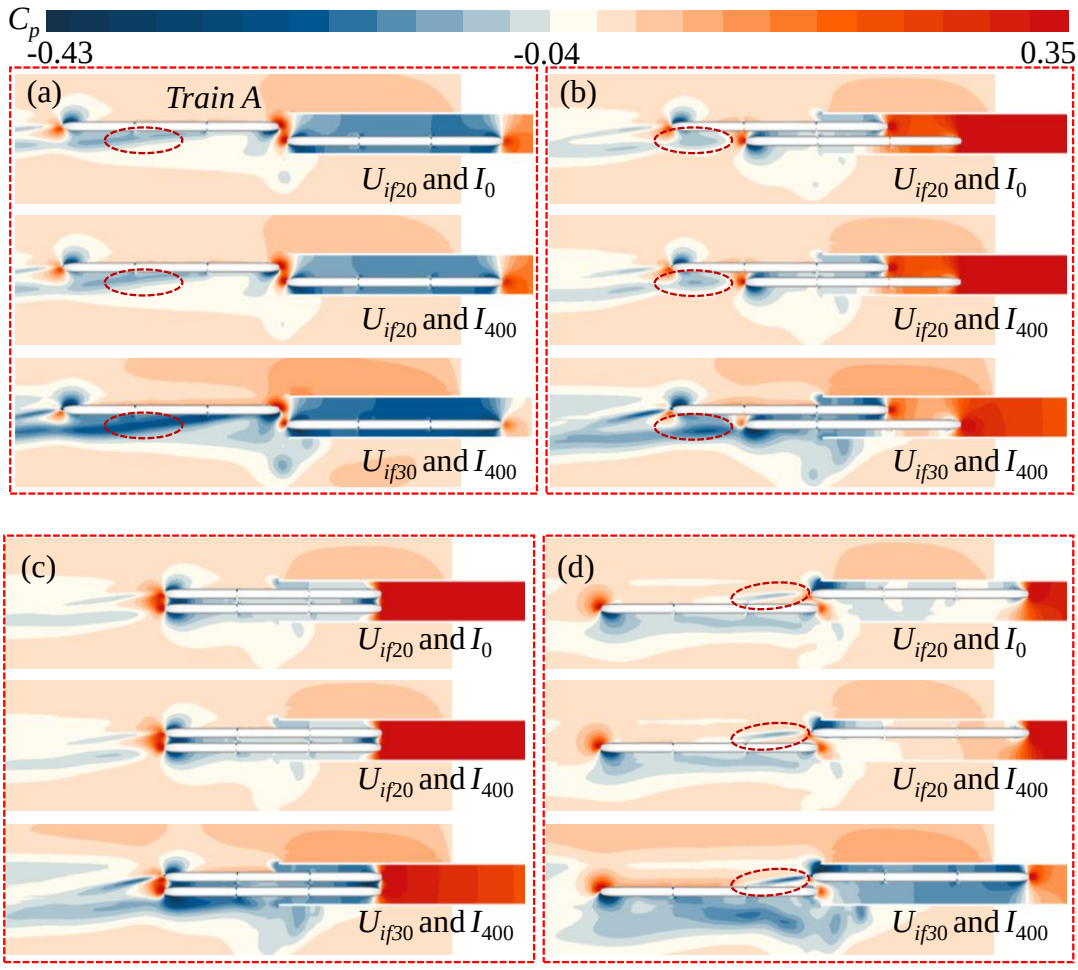

Fig. 12. Horizontal pressure field at different characteristic positions of the meeting process: (a) X=0 L; (b) X=1 L; (c) X=1.5 L; (d) X=3 L.

According to the analysis of Figs. 13~15, it can be further known that the windward side of the train body belongs to the positive pressure area under wind-rain environments. At the junction between the windward side and the train roof, the pressure changes from positive pressure to negative pressure, which is caused by the acceleration of the incoming flow on the top of the train. At the junction between the roof and the leeward side, although the pressure is still negative, its negative pressure strength weakens to a certain extent. In addition, from the head train to the tail train, it can be found that the center of negative pressure on the leeward side is constantly moving away from the body.

The difference in the three working conditions is not only reflected in the leeward side's negative pressure area, but also has an obvious impact on the windward side's positive pressure area. For a single case, the pressure in the positive pressure zone of three carriages outside the tunnel decreases sequentially, and the leeward side's negative pressure increases sequentially. It is challenging to understand why the head train's lateral force is the greatest and the tail train's lateral force is the smallest in the time history curve when only the cross-sectional pressure is taken into account. This can be achieved by combining the pressure coefficient curve in Fig. 8 with the horizontal pressure cloud plot in Fig. 12(a). The vortex structure of the leeward side of the head train's cross-sectional section is less developed than that of the middle train, and its negative pressure value around the head train is slightly lower than that of the middle train. However, the high positive pressure on the windward side of the head train's nose tip and the leeward side's high negative pressure are the dominant factors that lead to the huge pressure difference of the head train. The head train's

lateral force is therefore larger than the middle train's under the influence of the incoming flow. Due to the wake flow, which is the opposite of the aerodynamic effect of the head train's nose tip, the tail train experiences negative pressure on its windward side and positive pressure on its leeward side, resulting in a lower lateral force than the middle train.

For the cross-sectional pressure difference of different working conditions, it can be clearly observed from the figure that the rain phase increase the pressure value in the positive pressure area. The main reason for this phenomenon is that the falling rain phase is affected by the incoming flow to give it a horizontal speed. When the rain phase impacts on the train's windward side, part of the energy of the rain phase is lost and part of it increases the positive pressure due to momentum exchange (Yu et al., 2021). In addition, combined with the spatial distribution of rain phase and the pressure cloud map in Fig. 13, it can be found that the rain phase concentrated on the head train's leeward side increases the negative pressure value at the corresponding position. The rain phase distributed in the head train's leeward side increases the negative pressure intensity in the corresponding position, while the volume fraction of rain phase in the middle and tail trains' leeward sides is close to zero, but the vortex structure in the corresponding position is affected by the around flow, and the negative pressure increases.

It can be found that the volume fraction of the rain phase distributed in the head train's leeward side gradually decreases under the meeting, and it is difficult to observe a significant rain phase distribution at the X=1.5 L position. This is mainly because the head train entering the tunnel is not replenished by the rain phase, and the rain phase that was originally attached to the train body under the action of the slipstream gradually separates from the train. It is worth noting that in slice 2 of Figs.

14 and 15, it can be found that the rain phase's volume fraction around the train B at a wind speed of 30 m/s has increased significantly, mainly because the tunnel entrance's obstruction of the incoming flow causes a rise in flow near the entrance, which raises the volume fraction of the rain phase. When the train enters and leaves the tunnel in wind-rain environments, this phenomenon can further worsen the train's aerodynamic performance.

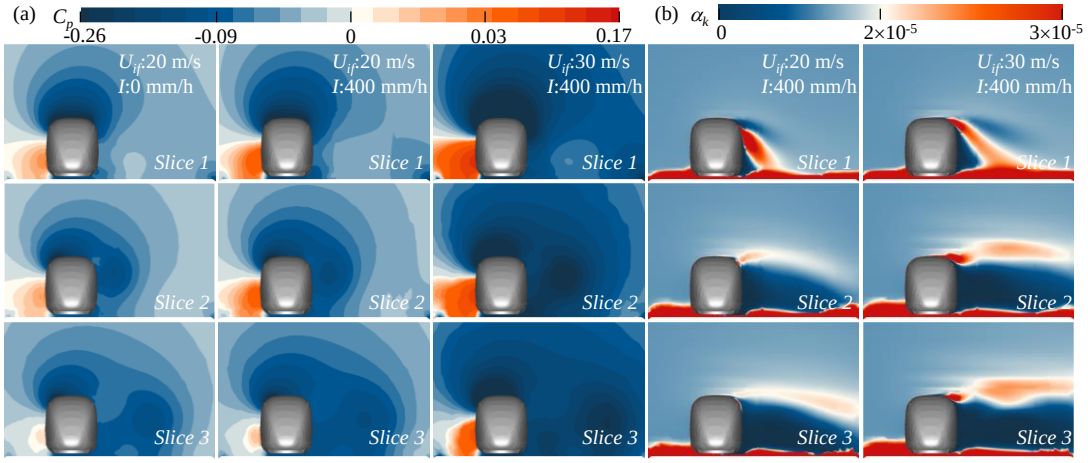

Fig. 13. Cross-sectional pressure and volume fraction at X=0 L: (a) pressure field at different slices; (b) the rain phase's volume fraction at different slices.

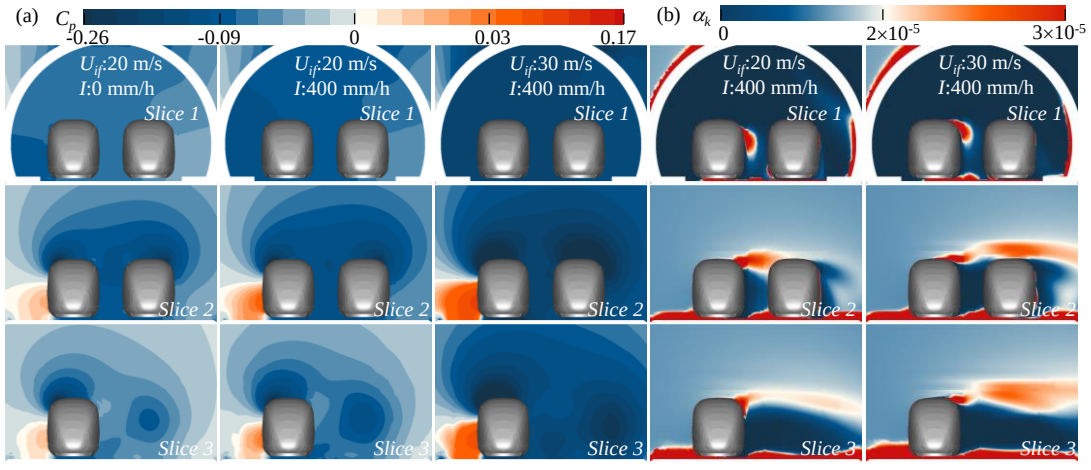

Fig. 14. Cross-sectional pressure and volume fraction at X=1 L: (a) pressure field at different slices; (b) the rain phase's volume fraction at different slices.

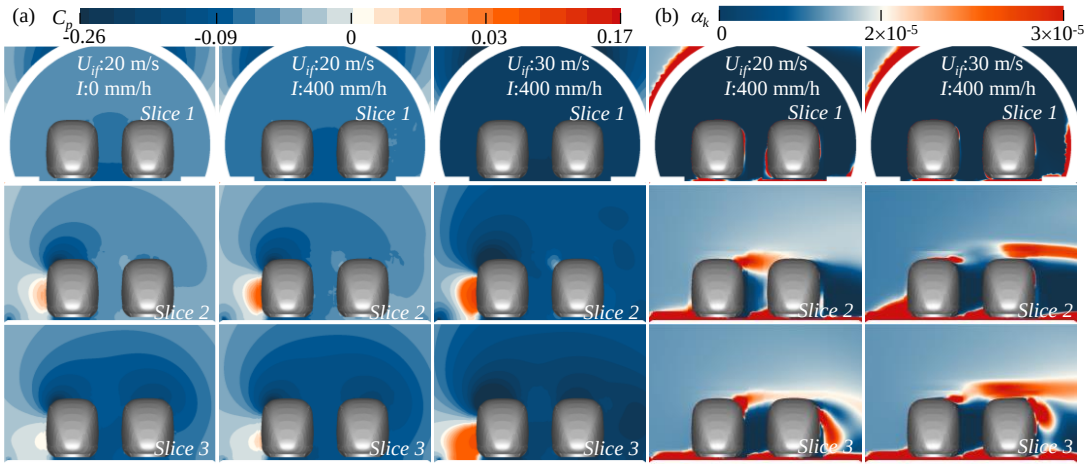

723

724 **Fig. 15.** Cross-sectional pressure and volume fraction at X=1.5 L: (a) pressure field at
725 different slices; (b) the rain phase's volume fraction at different slices.

726 # 5. Conclusions and future works

727 This paper focuses on the aerodynamic characteristic of trains meeting at tunnel-
728 embankment section under different rainfall intensities and wind speed conditions by
729 the Eulerian multiphase and SST k-ω models. The rain phase's spatial distribution
730 around the train under different cases and the influence mechanism of the rain phase
731 on the pressure field around the train are revealed by the flow field. The main
732 conclusions are as follows:

733 1. When the train runs alone on the embankment, the average wind-rain loads of
734 the train are higher than those in the pure crosswind (except for the tail train's lateral
735 force and the middle train's rolling moment). For head train, the $\overline{C}_y$, $\overline{C}_{my}$ and $\overline{C}_{mz}$
736 increased by 6.25%, 9.68% and 10.31%, respectively, under U_{if20} and I_{400}.

737 2. The pulsating pressure between the two trains dominates the train's wind-rain
738 loads under wind-rain environments, and the rain phase has a certain amplification
739 effect on the amplitude of some wind-rain loads. The ΔC_{mz} of the head, middle and
740 tail trains increased by 10.7%, 10.1% and 13.7%, respectively. When the train is in a
741 critical wind speed environment, the amplification effect of the rain phase on wind-

742 rain loads may cause the train's dynamic response index to exceed the limit.

743 3. Moment is more sensitive than force with the increase of rainfall intensity, the
744 change rate of $\overline{C}_{mz}$ reaches 4.9 times that of $\overline{C}_{y}$, the change rate of ΔC_{mz} is 4.8 times
745 that of ΔC_{y}; the average wind-rain force change rate is higher than that of wind-rain
746 moment with a rise in wind speed, the change rate of $\overline{C}_{y}$ reaches 3.4 times that of $\overline{C}_{mz}$;
747 no similar law is found in the change law of wind-rain amplitude and wind speed,
748 which may be caused by the influence of the meeting.

749 4. The distinction in the rain phase's spatial distribution between various wind
750 speed and rainfall intensity conditions is mainly reflected on the head train's leeward
751 side, and there is no significant difference between the middle and tail trains. The rain
752 phase on the head train's leeward side can be divided into four regions according to
753 the difference of volume fraction.

754 5. The rain phase increases the positive pressure on the head train's windward
755 side and the leeward side's negative pressure and turbulence intensity, which
756 promotes the vortex structure of the middle and tail trains away from the carriage.

757 In this paper, the spatial distribution of rain phase around the train and the
758 influence mechanism of rain on the flow field around the train are determined, and the
759 sensitivity of different wind-rain loads to the increase of wind speed and rainfall
760 intensity under different operating conditions (one vehicle or two trains meeting) is
761 analyzed. But the current research work is that there is still some room for further
762 exploration.

763 1. In the process of rainfall, the rain phase is composed of raindrop with different
764 particle sizes, so determining the spatial distribution of raindrops with different
765 particle sizes around the train and their contribution to the aerodynamic force of the
766 train can provide guidance for subsequent researchers in the selection of rain phase.

2. This paper only discusses and analyzes the transient aerodynamic performance of trains under different wind speed and rainfall intensity. The next work we need to do is the dynamic response index and driving safety under wind and rain environment. This is conducive to the safety evaluation of high-speed train running in rainy days at the tunnel entrance.

3. Under wind and rain environment, a water film will be attached to the track surface. For the operation scenarios such as tunnel and embankment, dry rail surface inside the tunnel and wet rail surface outside the tunnel are bound to occur. The existence of water medium between wheel and rail will affect the creep force and other indicators. Therefore, it has a broad prospect to study the influence of wheel-rail dry and wet conversion conditions on vehicle running safety at tunnel entrance.

CRediT authorship contribution statement

De-Hui Ouyang: Software, Writing–original draft, Data processing. E Deng: Methodology, Data curation, Writing–review & editing, Supervision, Funding acquisition, Project administration. Yi-Qing Ni: Resources, Writing–review & editing, Funding acquisition. Wei-Chao Yang: Conceptualization, Writing–review & editing. Zheng-Wei Chen: Writing–review & editing.

Declaration of Competing Interest

The authors declare that they have no known competing financial interests or personal relationships that could have appeared to influence the work reported in this paper.

Data availability

Data will be made available on request.

Acknowledgment

This work was funded by the National Natural Science Foundation of China

[grant numbers 51978670], the Research Grants Council, University Grants Committee of the Hong Kong Special Administrative Region (SAR), China [grant number R-5020-18], the Innovation and Technology Commission of the Hong Kong SAR Government [grant number K-BBY1] and The Hong Kong Polytechnic University's Postdoc Matching Fund Scheme [grant number 1-W21Q]. The work described in this paper was supported by a grant from the Guangdong Basic and Applied Basic Research Fund for Guangdong-Hong Kong-Macao Research Team Project (Grant No.2021B1515130006).

References

Andersson, E., Häggström, J., Sima, M., Stichel, S., 2004. Assessment of train-overturning risk due to strong cross-winds. Proc. Inst. Mech. Eng. Part F-J. Rail Rapid Transit 218(3), 213-223.

BS EN, 2013. Railway applications - aerodynamics-Part5: requirements and test procedures for aerodynamics in tunnels. BS EN 14067-4, 21-22.

Bocciolone, M., Cheli, F., Corradi, R., Muggiasca, S., Tomasini, G., 2008. Crosswind action on rail vehicles: Wind tunnel experimental analyses. J. Wind Eng. Ind. Aerodyn. 96(5), 584−610.

Chen, Z.W., Liu, T.H., Jiang, Z.H., Guo, Z.J., Zhang, J., 2018. Comparative analysis of the effect of different nose lengths on train aerodynamic performance under crosswind. J. Fluids Struct. 78, 69-85.

Chen, H., Furuya, T., Fukagai, S., Saga, S., Ikoma, J., Kimura, K., Suzumura, J., 2020. Wheel slip/Slide and low adhesion caused by fallen leaves. Wear. 446-447, 203187.

Dorigatti, F., Sterling, M., Baker, C.J., Quinn, A.D., 2015. Crosswind effects on the stability of a model passenger train—A comparison of static and moving

817 experiments. J. Wind Eng. Ind. Aerodyn. 138, 36–51.
818 Gou, H.Y., Li, W.H., Zhou, S.Q., Bao, Y., Zhao, T.Q., Han, B., Pu, Q.H., 2021.
819 Dynamic Response of High-Speed Train-Track-Bridge Coupling System Subjected
820 to Simultaneous Wind and Rain. Int. J. Struct. Stab. Dyn. 21 (11), 2150161.
821 Gunn, R., Kinzer, G.D., 1949. The terminal velocity of fall for water droplets in
822 stagnant air. Journal of Meteorology 6, 243–248.
823 Kubilay, A., Derome, D., Blocken, B., Carmeliet, J., 2015. Wind-driven rain on two
824 parallel wide buildings: Field measurements and CFD simulations. J. Wind Eng. Ind.
825 Aerodyn. 146, 11–28.
826 Hu, H., Xiang, H.Y., Liu, K.H., Zhu, J., Li, Y.L., 2022. Aerody-namic characteristics
827 of moving vehicles of two trains passing each other on bridge under crosswinds. J.
828 Cent. South Univ. 29, 2558–2573.
829 Huang, S.H., Li, Q.S., 2012. Large Eddy Simulations of Wind-Driven Rain on Tall
830 Building Facades. J. Struct. Eng. 138, 967-983.
831 Huang, S.H., Li, Q.S., Liu, M., Chen, F.B., Liu, S., 2019. Numerical Simulation of
832 Wind-Driven Rain on a Long-Span Bridge. Int. J. Struct. Stab. Dyn. 19(12),
833 1950149.
834 Han, Y., Liu, Y., Hu, P., Cai, C.S., Xu, G.J., Huang, J.Y., 2020. Effect of unsteady
835 aerodynamic loads on driving safety and comfort of trains running on bridges.
836 Adv. Struct. Eng. 23(13), 2898-2910.
837 Krajnovic´, S., Ringqvist, P., Nakade, K., Basara, B., 2012. Large eddy simulation of
838 the flow around a simplified train moving through a crosswind flow. J. Wind Eng.
839 Ind. Aerodyn. 110, 86–99.
840 Kubilay, A., Derome, D., Blocken, B., Carmeliet, J., 2013. CFD simulation and
841 validation of wind-driven rain on a building facade with an Eulerian multiphase

model. Build. Environ. 61, 69-81.

Li, T., Zhang, J., Rashidi, M., Yu, M., 2019. On the Reynolds-Averaged Navier-Stokes Modelling of the Flow around a Simplified Train in Crosswinds. J. Appl. Fluid Mech. 12 (2), 551-563.

Liu, K., Wang, M., Zhou, T.J., 2021. Increasing costs to Chinese railway infrastructure by extreme precipitation in a warmer world. Transportation Research Part D., 93 (2021) 102797.

Li, T., Liang, H., Zhang, J., Zhang, J., 2023. Numerical Study on Aerodynamic Resistance Reduction of High-speed Train Using Vortex Generator. Eng. Appl. Comp. Fluid Mech. 17(1), 9-20.

Liang, H., Sun, Y.C., Li, T., Zhang, J.Y., 2023. Influence of marshalling length on aerodynamic characteristics of urban EMUs under crosswind. J. Appl. Fluid Mech. 16(1), 9-20.

Jiang, C. W., Xu, C. H., Gao, Z. X., Lee, C. H., 2016. Finite panel method for the simulation of wind–driven rain. Build. Environ. 2016, 105: 358–368.

Jian, Z.M., Wang, Y., Dang, H.W., Mohtadi, M., Rosenthal, Y., Lea, D.W., Liu, Z.F., Jin, H.Y., Ye, L.M., Kuhnt, W., Wang, X.X., 2022. Warm pool ocean heat content regulates ocean–continent moisture transport. Nature. 612, 92–99.

Menter, F.R., 1994. Two-equation Eddy-viscosity turbulence model for engineering applications. AIAA J. 32, 1598-1605.

Montenegro, P.A., Heleno, R., Carvalho, H., Calcada, R., Baker, C.J., 2020(a). A comparative study on the running safety of trains subjected to crosswinds simulated with different wind models. J. Wind Eng. Ind. Aerod. 207, 104398.

Montenegro, P.A., Calçada, R., Carvalho, H., Bolkovoy, A., Chebykin I., 2020(b). Stability of a train running over the Volga river high-speed railway bridge during

crosswinds. Struct. Infrastruct. Eng. 16(8), 1121-1137.

Mohebbi, M., Baboli M.A.R., 2013. Numerical Calculations of Aerodynamic Performance an Regional Passenger Train at Crosswind Conditions. Int. J. Vehicle Structures & Systems 5(2), 68-74.

Mohebbi, M., Rezvani, M.A., 2017. Two-dimensional analysis of the influence of windbreaks on airflow over a high-speed train under crosswind by using Lattice Boltzmann Method. Proc. Inst. Mech. Eng. Part F-J. Rail Rapid Transit 232(3), 863-872.

Mohebbi, M., Rezvani, M.A., 2018a. Multi objective optimization of aerodynamic design of high speed railway windbreaks using lattice boltzmann method and wind tunnel test results. Int. J. Rail Transp. 6(3), 183-201.

Mohebbi, M., Rezvani, M.A., 2018b. The Impact of Air Fences Geometry on Air Flow around an ICE3 High Speed Train on a Double Line Railway Track with exposure to Crosswinds. J. Appl. Fluid Mech. 11(3), 743-754.

Mohebbi, M., Rezvani, M.A., 2021. 2D and 3D numerical and experimental analyses of the aerodynamic effects of air fences on a high-speed train. Wind Struct. 32(6), 539-550.

Mohebbi, M., Safaee, A.M., 2022. The optimum model determination of porous barriers in high-speed tracks. Proc. Inst. Mech. Eng. Part F-J. Rail Rapid Transit 236(1), 15-25.

Noguchi, Y., Suzuki, M., Baker, C., Nakade, K., 2019. Numerical and experimental study on the aerodynamic force coefficients of railway vehicles on an embankment in crosswind. J. Wind Eng. Ind. Aerod. 184, 90-105.

Neto, J., Montenegro, P.A., Vale, C., Calçada, R., 2021. Evaluation of the train running safety under crosswinds - a numerical study on the influence of the wind

speed and orientation considering the normative Chinese Hat Model. Int. J. Rail Transp. 9(3), 204-231.

Ottar, T., Egle, S., Kristiina, R., Jaak, J., Toomas, T., 2023. The intensification of short-duration rainfall extremes due to climate change – Need for a frequent update of intensity–duration–frequency curves. Climate Services. 30, 100349.

Ouyang, D.H., Yang, W.C., Deng, E, Wang, Y.W., He, X.H., Tang, L.B., 2023. Comparison of aerodynamic performance of moving train model at bridge–tunnel section in wind tunnel with or without tunnel portal. Tunn. Undergr. Space Technol. 135, 105030.

Rezvani, M.A., Mohebbi, M., 2014. Numerical calculations of aerodynamic performance an atm train at crosswind conditions. Wind Struct. 18(5), 529-548.

Shao, X.M., Wan, J., Chen, D.W., Xiong, H.B., 2011. Aerodynamic modeling and stability analysis of a high-speed train under strong rain and crosswind conditions. J. Zhejiang Univ. Sci. A. 12, 964–970.

Wolf, D., 2001. On the Laws-Parsons distribution of raindrop size. Radio Scienc. 36 (4), 639-642.

Wang, X., Qian, Y.H., Chen, Z.S., Zhou, X., Huang, H.L., 2019. Numerical studies on aerodynamics of high-speed railway train subjected to strong crosswind. Adv. Mech. Eng. 11 (11), 1–12.

Wang, L., Luo, J.J., Li, F.L., Guo, D.L., Gao, L.P., Wang, D.K., 2021. Aerodynamic performance and flow evolution of a high-speed train exiting a tunnel with crosswinds. J. Wind Eng. Ind. Aerodyn. 218, 104786.

Wu, B., Xiao, G.W., An, B.Y., Wu, T., Shen, Q., 2022. Numerical study of wheel/rail dynamic interactions for high-speed rail vehicles under low adhesion conditions during traction. Eng. Fail. Anal. 137, 106266.

Yu, M.G., Liu, J.L., Dai, Z.Y., 2021. Aerodynamic characteristics of a high-speed train exposed to heavy rain envioronment based on non-spherical raindrop. J. Wind Eng. Ind. Aerod. 211, 104532.

Yu, M.G., Sheng, X.G., Liu, J.L., Huo, W., Li, M.X., 2022. Effects of wind-rain coupling on the aerodynamic characteristics of a high-speed train. J. Wind Eng. Ind. Aerod. 231, 105213.

Yang, X.M., Wang, X.X., Cai, Z.Y., Cao, W.M., 2021. Detecting spatiotemporal variations of maximum rainfall intensities at various time intervals across Virginia in the past half century. Atmospheric Research. 255, 105534.

Yang, W.C., Liu, Y.K., Deng, E. Wang, Y.W., He, X.H., Lei, M.F., Zou, Y.F., 2022a. Field test and numerical reconstitution of natural winds at the tunnel entrance section of high-speed railway. Int. J. Numer. Methods Heat Fluid Flow. 33(2), 617-647.

Yang, W.C., Ouyang, D.H., Deng, E., Wang, Y.W., Chen, Z.W., He, X.H., Huang. Y.M., 2022b. Deterioration of aerodynamic performance of a train driving through noise barriers under crosswinds. J. Wind Eng. Ind. Aerod. 231, 105241.

Yang, W.C., Liu, Y.K., Deng, E., Wang, Y.W., He, X.H., Lei, M.F., 2022c. Measurement. 202, 111806.

Zhou, L., Liu, T.H., Chen, Z.W., Li, W.H., Guo, Z.J., He, X.H., Wang, Y.W., 2021. Comparison study of the effect of bridge-tunnel transition on train aerodynamic performance with or without crosswind. Wind Struct. 32(6), 597-612.

Zeng, G.Z., Li, Z.W., Huang, S., Chen, Z.W., 2023. Influence of wind and rain environment on operational safety of intercity train running on the viaduct. Int. J. Numer. Methods Heat Fluid Flow 33(4), 1584-1608.